

Effect of Marangoni forces on interfacial heat and mass transfer driven by surface cooling

Herlina Herlina¹  and Jan Wissink^{1,2} 

¹Institute for Water and Environment, Karlsruhe Institute of Technology, Kaiserstr.12, 76131 Karlsruhe, Germany

²MAE Department, Brunel University of London, Kingston Lane, Uxbridge UB8 3PH, UK

Corresponding author: Herlina Herlina, herlina.herlina@kit.edu

(Received 15 May 2025; revised 12 November 2025; accepted 12 November 2025)

A fully resolved numerical study was performed to investigate interfacial heat and mass transfer enhanced by the fully developed Rayleigh–Bénard–Marangoni instability in a relatively deep domain. The instability was triggered by evaporative cooling modelled by a constant surface heat flux. The latter allowed for temperature-induced variations in surface tension giving rise to Marangoni forces reinforcing the Rayleigh instability. Simulations were performed at a fixed Rayleigh number (Ra_h) and a variety of Marangoni numbers (Ma_h). In each simulation, scalar transport equations for heat and mass concentration at various Schmidt numbers ($Sc = 16–200$) were solved simultaneously. Due to the fixed (warm) temperature prescribed at the bottom of the computational domain, large buoyant plumes emerged quasi-periodically both at the top and bottom. With increasing Marangoni number a decrease in the average convection cell size at the surface was observed, with a simultaneous improvement in near-surface mixing. The presence of high aspect ratio rectangular convection cell footprints was found to be characteristic for Marangoni-dominated flows. Due to the promotion of interfacial mass transfer by Marangoni forces, the power in the scaling of the mass transfer velocity, $K_L \propto Sc^{-n}$, was found to decrease from $n = 0.50$ at $Ma_h = 0$ to ≈ 0.438 at $Ma_h = 13.21 \times 10^5$. Finally, the existence of a buoyancy-dominated and a Marangoni-dominated regime was investigated in the context of the interfacial heat and mass transfer scaling as a function of $Ma_h + \varepsilon Ra_h$, where ε is a small number determined empirically.

Key words: buoyancy-driven instability, marangoni convection, air/sea interactions

1. Introduction

It is well known that surface water is a very important buffer for the (temporary) storage of heat and atmospheric gases (Johnson *et al.* 2021; Cheng *et al.* 2022; Gruber *et al.* 2023; Pan *et al.* 2023). Hence, a proper understanding of the heat and gas transfer across the air–water interface is of fundamental importance to reliably predict the global heat and greenhouse gas budget (Yu 2019). The very low mass diffusivity D of atmospheric gases in water, combined with their typically low to moderate solubility, gives rise to very steep concentration gradients throughout the water phase. Especially at the surface this leads to a very thin concentration boundary layer that is extremely difficult to fully resolve both in experiments and in numerical simulations. Because of this, to date, in many direct numerical simulations (DNS) the Schmidt number $Sc = \nu/D$, where ν is the kinematic viscosity, was often limited to values below 50 (e.g. Schwertfimer & Manhart 2007; Nagaosa & Handler 2012; Tsai *et al.* 2013). Note that for atmospheric gases dissolved in water, the Schmidt number in typical ambient temperature conditions varies between 100 and 1000, for instance, at 20 °C the Schmidt number for helium is $Sc \approx 150$, for oxygen it is $Sc \approx 500$ and for carbon dioxide it is $Sc \approx 600$ (see, e.g. Jähne & Haassecker 1998).

Interfacial heat and mass transfer at the air–water interface is enhanced by various turbulence generating mechanisms, which often reinforce one another. The most prominent one is turbulence induced by wind shear directly at the surface (Zappa *et al.* 2007; Wanninkhof 2014; Garbe *et al.* 2014; Kurose *et al.* 2016; Turney 2016; Blomquist *et al.* 2017; Komori *et al.* 2018). In, for example, streams and rivers, bottom-shear induced turbulence, as studied by Magnaudet & Calmet (2006), Herlina & Jirka (2008); Huotari *et al.* (2013), Turney & Banerjee (2013), Variano (2013), Herlina & Wissink (2014), Pinelli *et al.* (2022), is prevalent. Finally, turbulence in the water phase can also be generated by surface cooling induced instabilities, e.g. due to evaporation (Shay & Gregg 1984; Soloviev & Klinger 2001; Podgrajsek, Sahlee & Rutgersson 2014; Ali 2020). The latter effect usually dominates at very low wind speeds in more or less stagnant water (Rutgersson & Smedman 2010; MacIntyre *et al.* 2018, 2021).

Turbulence generated by surface cooling effects can give rise to (deeply penetrating) buoyant convection (Schladow *et al.* 2002; Jirka, Herlina & Niepelt 2010; Wissink & Herlina 2016) that often acts in concert with surface-temperature-gradient-induced Marangoni forces (Nield 1964; Toussaint *et al.* 2008). At the surface this process typically results in the appearance of a pattern of convection cell footprints, such as studied by Pearson (1958), Bodenschatz, Pesch & Ahlers (2000), Nepomnyashchy, Legros & Simanovskii (2006), Schwarzenberger *et al.* (2014), Köllner *et al.* (2016).

It should be noted that Marangoni effects can also be generated by local concentration variations in a multicomponent fluid (e.g. Schwarzenberger *et al.* 2014). For instance, in binary droplets, evaporation of the more volatile component induces density differences as well as surface tension gradients (see Diddens, Li & Lohse (2021) and the references therein). Another example is the Marangoni force induced by surfactant-concentration gradients as studied by, e.g. Khakpour, Shen & Yue (2011) and Wissink *et al.* (2017). The latter study showed a gradual decrease in interfacial mass transfer with increasing surfactant concentration. In the natural world, surface tension effects are generally induced by a combination of surface-temperature and solutal-concentration gradients. To gain a fundamental understanding of the effectiveness and intricacies of the individual heat and gas transfer mechanisms, however, a first step is to study each case in isolation.

Traditionally, chemical engineering applications have been a major driving force for Marangoni-instability studies, usually focusing on droplets and/or shallow domains bounded from below by a solid wall (e.g. Koschmieder & Prahl 1990;

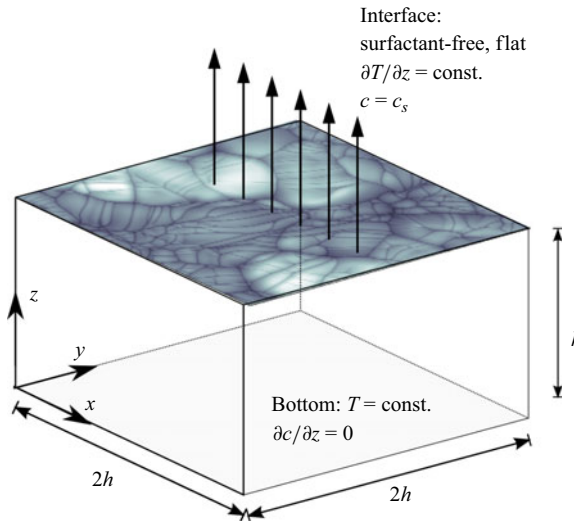


Figure 1. Schematic of computational domain. Evaporative cooling was modelled by a constant heat flux $\partial T / \partial z$ at the surface. The concentration c at the surface was assumed to be at saturation ($c = c_s$) at all times. Periodic boundary conditions were employed in the horizontal directions.

Toussaint *et al.* 2008; Schwarzenberger *et al.* 2014; Diddens *et al.* 2021; Dhas, Roy & Toppaladoddi 2023). Contrastingly, studies in relatively deep domains are much less common (Spangenberg & Rowland 1961; Davenport 1972; Tan & Thorpe 1996; Flack, Saylor & Smith 2001). Recently, in (Wissink & Herlina 2023) a detailed parameter study was presented to investigate the combined influence of buoyancy and surface-temperature-induced Marangoni effects in the case of a developing Rayleigh–Bénard–Marangoni (RBM) instability in a deep domain. To this end, a number of simulations were performed for varying Rayleigh and Marangoni numbers. The analysis focused on the initial development of the instability until the moment that the first plumes started to plummet. It was shown that the Marangoni and buoyant instabilities reinforce one another, leading to a rapid development of the RBM instability for high Rayleigh and/or Marangoni numbers. The results show that in the case of evaporative cooling it is incorrect to discard the Marangoni instability, which was found to significantly contribute to near-surface mixing.

In contrast to the aforementioned developing RBM cases, the present paper extends the study to interfacial heat and mass transfer in the presence of a fully developed RBM instability. This includes the influence of quasi-periodic buoyant plumes generated by the Rayleigh instability at the bottom of the domain. To this end, fully resolved, time-accurate DNS were performed. A schematic of the computational domain is shown in figure 1. The set-up of the simulations was inspired by the buoyant-convectively driven gas transfer experiments conducted at the Karlsruhe Institute of Technology (Jirka *et al.* 2010; Murniati *et al.* 2025) and somewhat resembles the situation encountered immediately below the water surface of a quiescent lake. The simulations aim to help explain the unexpectedly high interfacial heat and gas transfer detected at low wind speeds (see, e.g. MacIntyre, Amaral & Melack 2021). Further aims of this paper are to elucidate, e.g. the effect of surface-temperature-induced Marangoni forces on surface and bulk temperature, convection cell topology and the scaling of the heat and mass transfer with Schmidt number and convection cell size. To achieve this, in the simulations the Marangoni number was varied, while the Rayleigh number was kept constant.

Ideally, for a detailed description of evaporative cooling effects, both the water and air phase would need to be simulated simultaneously, as the evaporative-induced cooling changes locally with the relative humidity of the overlying air. As such simulations are very expensive, it was decided to reduce the (computational) complexity by only simulating the water phase and model the evaporative cooling by a constant surface heat flux. The latter allows for a non-uniform surface-temperature distribution, generating surface-temperature-gradient-induced Marangoni forces. To subsequently obtain a fully developed RBM flow, a constant temperature was prescribed at the bottom boundary.

The interfacial mass transfer of dissolved gases was modelled by assuming that the concentration at the interface is at saturation at all times. This was combined with a zero normal flux for the concentration at the bottom (see also § 2.4). Normal ambient conditions were assumed with dissolved gas concentrations that do not alter significantly the surface tension nor the density of water. These assumptions hold for most atmospheric gases such as helium, oxygen, nitrogen and carbon dioxide. Hence, the dissolved gas concentrations were represented by passive scalars that were solved simultaneously with the time-dependent flow equations. The latter allows for a non-biased study of the Schmidt number effects on the scalar fields.

While the mesh needs to be sufficiently fine to accurately resolve the extremely steep concentration gradients associated with the high Sc numbers, the computational domain needs to be sufficiently large to accommodate the large length scale associated with the quasi-periodic buoyant plumes generated at the top and bottom of the domain. Simultaneously, the large time scale associated with the buoyant instability requires a significant simulation time in order to obtain sufficiently converged statistics. This makes the present simulations very challenging and time consuming. Because of the aforementioned considerations, the following actions were taken: (i) the horizontal size of the computational domain was chosen such that in the purely buoyancy-dominated case, on average, at least two large convection cells (often accompanied by a number of much smaller cells) could be conveniently accommodated, and (ii) Schmidt numbers up to $Sc = 200$ were considered (which includes the Schmidt number that is characteristic for helium dissolved in water). Results presented later in the paper suggest that various observations and scaling laws for the gas transfer velocities obtained for $50 \leq Sc \leq 200$ would also apply for $Sc > 200$. Where applicable, this will be highlighted in the discussion of the results.

2. Computational aspects

2.1. Governing equations

As mentioned above, this study addresses both heat and mass transfer across the air–water interface driven by surface cooling. Around a temperature of $T = 20$ °C, an almost linear dependency between water density and temperature exists. The typically small changes in density allow for the Boussinesq approximation to be employed to model the flow induced by the unstable stratification near the surface. Following Balachandar (1992), for the non-dimensionalisation of the Navier–Stokes equations, a reference length scale h and velocity scale $U_\kappa = \kappa/h$ were used, where κ is the thermal diffusivity and h is the depth of the computational domain. The resulting continuity equation, using the Einstein summation convention, reads

$$\frac{\partial u_i^*}{\partial x_i^*} = 0, \quad (2.1)$$

and the momentum equations are given by

$$\frac{\partial u_i^*}{\partial t^*} + \frac{\partial u_i^* u_j^*}{\partial x_j^*} = -\frac{\partial p^*}{\partial x_i^*} + Pr \frac{\partial^2 u_i^*}{\partial x_j^* \partial x_j^*} + Ra_h Pr T^* \delta_{i3}, \quad i = 1, 2, 3, \quad (2.2)$$

where x_1^* , x_2^* are the horizontal (x , y) directions and x_3^* is the vertical (z) direction, $u_1^* = u/U_\kappa$, $u_2^* = v/U_\kappa$ and $u_3^* = w/U_\kappa$ are the velocities in the x , y and z directions, respectively, p^* is the generalised pressure, t^* denotes time and $Pr = \nu/\kappa$ is the Prandtl number corresponding to the ratio of the momentum and thermal diffusivities, while the superscript ‘*’ denotes non-dimensionalisation using h and U_κ . The buoyancy force in the z direction is represented by the last term on the right-hand side of (2.2), in which δ_{i3} is the Kronecker delta,

$$Ra_h = \frac{\alpha q g h^4}{\kappa \nu} \quad (2.3)$$

is the modified Rayleigh number, where α is the thermal expansion factor and $g = -9.81$ m s⁻² is the gravitational acceleration, and finally,

$$T^* = \frac{(T_{bot} - T)}{qh} \quad (2.4)$$

is the non-dimensional temperature, where T_{bot} is the (constant) bottom temperature and $q = (\partial T/\partial z)|_s$ is the temperature gradient at the water surface, which is kept constant.

The three-dimensional convection–diffusion equation for T^* is given by

$$\frac{\partial T^*}{\partial t^*} + \frac{\partial u_j^* T^*}{\partial x_j^*} = \frac{\partial^2 T^*}{\partial x_j^* \partial x_j^*}. \quad (2.5)$$

Similarly, the passive scalar transport is governed by the convection–diffusion equation of the non-dimensional scalar concentration c^* ,

$$\frac{\partial c^*}{\partial t^*} + \frac{\partial u_j^* c^*}{\partial x_j^*} = \frac{Pr}{Sc} \frac{\partial^2 c^*}{\partial x_j^* \partial x_j^*}, \quad (2.6)$$

with

$$c^* = \frac{c - c_b(0)}{c_s - c_b(0)}, \quad (2.7)$$

where c_s is the (constant) saturation concentration at the surface and $c_b(0)$ denotes the initial bulk concentration at $t = 0$, where

$$c_b(t) = \frac{1}{h} \int_0^h \langle c(x, y, z, t) \rangle_{x,y} dz, \quad (2.8)$$

using $\langle \cdot \rangle_{x,y}$ to denote averaging in the horizontal (x , y) directions.

As in Wissink & Herlina (2023), the effect of surface-temperature-gradient-induced Marangoni forces on the horizontal velocity components was modelled by

$$\left. \frac{\partial u_i^*}{\partial x_3^*} \right|_s = -Ma_h \left. \frac{\partial T^*}{\partial x_i^*} \right|_s, \quad i = 1, 2, \quad (2.9)$$

where

$$Ma_h = \frac{(\mathrm{d}\sigma/\mathrm{d}T) q h^2}{\mu \kappa} \quad (2.10)$$

denotes the Marangoni number, in which σ and μ are the surface tension and dynamic viscosity, respectively. Note that (2.9) was derived from the surfactant-induced Marangoni model used by Wissink *et al.* (2017) and is equivalent to the model of Pearson (1958). For water at about 20 °C, $\kappa = 0.143 \times 10^{-6} \text{ m}^2 \text{s}^{-1}$, $\alpha = 0.000207 \text{ K}^{-1}$ and $d\sigma/dT = -0.000151 \text{ Nm}^{-1} \text{ K}^{-1}$. Except for $d\sigma/dT$ (which was varied between -0.000151 and $0 \text{ Nm}^{-1} \text{ K}^{-1}$), the (macro) Rayleigh and Marangoni numbers were based on the aforementioned values, along with the fixed $h = 0.05 \text{ m}$ and constant $q = -500 \text{ (K m}^{-1})$. The latter corresponds to a heat flux of approximately 300 Wm^{-2} .

2.2. Appropriate scales

In our previous study (Wissink & Herlina 2023), we focused on the effects of Marangoni forces on the initial development of the RBM instability, which is independent of the depth of the computational domain. Hence, the ‘initial’ length scale was chosen (arbitrarily) to be fixed at a value of $L = 0.01 \text{ m}$, while the ‘critical length scale’ was based on the thermal boundary layer thickness defined by

$$\delta_T(t) = \frac{\langle T_s(x, y, t) \rangle_{x,y} - T_b(t)}{q}, \quad (2.11)$$

where

$$T_b(t) = \frac{1}{h} \int_0^h \langle T(x, y, z, t) \rangle_{x,y} dz \quad (2.12)$$

denotes the bulk temperature and T_s is the surface temperature. For the developing RBM instability, both length scales (L and δ_T) were independent of the actual (much larger) depth of the computational domain.

Here, for the fully developed RBM instability, the depth (h) of the computational domain is the appropriate length scale only for the Rayleigh number. A proper length scale for the Marangoni number would be the mean thermal boundary layer thickness δ_T , which can only be determined *a posteriori*. Hence, the *a priori* determined Ma_h (2.10) was used in the computations. Based on this Ma_h , dimensional analysis suggests that

$$\delta_T \propto \delta_\sigma = \sqrt{\frac{\mu \kappa}{(d\sigma/dT) q}}, \quad (2.13)$$

where δ_σ is the *a priori* Marangoni length scale, which is proportional to $\sqrt{1/Ma_h}$, but is independent of h . Similarly, the typical Marangoni velocity scale reads

$$U_\sigma = \sqrt{\frac{(d\sigma/dT) q \kappa}{\mu}} \propto \sqrt{Ma_h}. \quad (2.14)$$

Analogously, based on Ra_h , an *a priori* Rayleigh length scale

$$\delta_R = \left(\frac{\kappa \nu}{\alpha g q} \right)^{0.25} \propto Ra_h^{-0.25} \quad (2.15)$$

and velocity scale

$$U_R = \frac{\alpha g q h^3}{\nu} \propto Ra_h \quad (2.16)$$

can be obtained. Note that U_R for a fully developed flow inherently depends on h .

Run	Ma_h	Base mesh size	Sc of passive scalar	Refinement
M0	0	$400 \times 400 \times 252$	16, 50, 100, 200	1, 2, 2, 3
M1	0.88×10^5	$400 \times 400 \times 252$	16, 50, 100, 200	1, 2, 3, 3
M2	1.76×10^5	$400 \times 400 \times 252$	—	—
M3	2.64×10^5	$400 \times 400 \times 252$	—	—
M5	4.40×10^5	$400 \times 400 \times 252$	16, 50, 100, 200	2, 3, 4, 5
M10	8.81×10^5	$800 \times 800 \times 504$	16, 50, 100, 200	1, 2, 3, 4
M12	11.01×10^5	$800 \times 800 \times 504$	—	—
M15	13.21×10^5	$800 \times 800 \times 504$	16, 50, 100, 200	2, 2, 3, 4

Table 1. Simulation parameters. In all simulations, the domain size was $2h \times 2h \times h$, $Pr = 7$, $Ra_h = 4.44 \times 10^7$, $(\partial T^* / \partial z^*)|_s = -1$.

2.3. Numerical method

The simulations were performed using the in-house KCFlo solver described in Kubrak *et al.* (2013). The solver was specifically designed to generate fully resolved subsurface velocity and scalar fields for high-Schmidt-number (low-diffusivity) mass transfer processes at the air–water interface. In this solver the discretisation of the three-dimensional incompressible Navier–Stokes equations uses a fourth-order-accurate central discretisation of the diffusion terms, combined with a fourth-order central kinetic energy conserving discretisation (Wissink 2004) of the convective terms. The Poisson equation for the pressure is solved using a conjugate gradient solver with simple diagonal preconditioning. For the discretisation of the scalar convection and diffusion, the fifth-order-accurate weighted essentially non-oscillatory scheme of Liu, Osher & Chan (1994) and a fourth-order-accurate central method are employed, respectively. A staggered Cartesian non-uniform mesh arrangement was used, where the velocities are defined in the middle of the cell faces, while all scalars (temperature, pressure and concentration) are defined in the centre of the grid cells. The time integration of the velocity and the scalar fields were performed using the second-order-accurate Adams–Bashforth method.

As the temperature is an active scalar and directly affects the velocity, it is essential to solve both on the same (base) mesh. To further increase the accuracy of the scalar discretisation, the solver allows the usage of refined meshes, where scalar fields are solved on a finer mesh than the flow field (see also Kubrak *et al.* 2013). A divergence-free instantaneous velocity field on each of the refined meshes was obtained by performing the following steps. First, a fourth-order-accurate interpolation of the u^* , v^* components of the velocity field to the refined mesh was carried out. Second, this u^* , v^* field was employed to reconstruct the w^* -velocity field by using the second-order central discretisation of the continuity equation starting with the interfacial boundary condition $w^* = 0$ and subsequently moving downwards grid plane by grid plane.

The simulations presented in this paper comprised medium- to large-scale computations (cf. table 1). The code was parallelised by splitting the computational domain into blocks of equal size. Communication between blocks was performed using the standard message passing interface protocol. For the largest simulation, up to 20.644×10^9 grid points and 4800 cores were used.

2.4. Computational set-up, boundary and initial conditions

The simulations were performed at a fixed Rayleigh number ($Ra_h = 4.44 \times 10^7$) combined with a wide range of Marangoni numbers ($Ma_h = 0$ to $Ma_h = 13.21 \times 10^5$). The $2h \times 2h \times h$ computational domain (cf. figure 1) was discretised using a $400 \times 400 \times 252$ base

mesh for the cases with $Ma_h \leq 4.40 \times 10^5$ and a $800 \times 800 \times 504$ base mesh for $Ma_h \geq 8.81 \times 10^5$. To attain a finer resolution near the interface, the mesh was stretched using the node distribution

$$z(k) = \left[1 - \frac{\tanh(z_p)}{\tanh(\psi/2)} \right] z(0)/2 + \left[1 + \frac{\tanh(z_p)}{\tanh(\psi/2)} \right] z(n_z)/2 \quad (2.17)$$

for $k = 1, \dots, n_z - 1$, with $\psi = 2$ and

$$z_p = \psi \left[\frac{k}{n_z} - 0.5 \right], \quad (2.18)$$

where $z(n_z) - z(0) = h$ is the vertical extent of the computational domain and n_z is the number of nodes in the z direction. In parallel to the flow and temperature fields, in each simulation up to four passive scalar fields with different Schmidt numbers were solved simultaneously. The latter allowed an unbiased parametric study of the Schmidt number dependency of the mass transfer velocity K_L . As mentioned in § 2.3, when required, a refined mesh was employed in order to accurately resolve the higher- Sc concentration fields. An overview of the simulations, including the respective scalar mesh refinement factors used, is provided in table 1. Note that the results of a rigorous grid refinement study that was performed to evaluate the quality of the mesh are presented in Appendix A.

In the horizontal directions of the computational domain, periodic boundary conditions were employed for all variables. As discussed in § 1, to mitigate possible effects of lateral confinements, the chosen domain size (in combination with the chosen Rayleigh number) was such that at least two (large) convection cells could be conveniently accommodated. At the bottom, free-slip boundary conditions were imposed. The surface was assumed to be flat with a vertical velocity of zero, while the horizontal velocities were modelled using (2.9). This rigid lid assumption can only be justified *a posteriori* by, e.g. calculating the Crispation ($Cr = \rho v \kappa / \sigma \delta_T$) and Galileo ($Ga = |g \delta_T^3 / \nu \kappa|$) numbers for each simulation using the thermal boundary layer thickness δ_T as the characteristic length scale. It was found that Cr ranges from 2.04×10^{-6} to 6.18×10^{-6} and Ga ranges from 2.2×10^3 to 6.12×10^4 . As in all simulations $Cr \ll 1$ and $Ga \gg 1$, the flat surface assumption employed here was justified.

As illustrated in figure 1, the heat flux at the top was kept fixed ($\partial T^* / \partial z^* = -1$), while at the bottom the temperature was kept constant ($T^* = 0$). Finally, for the passive scalar concentrations, at the bottom the scalar flux $\partial c^* / \partial z^*$ was set to zero. At the surface, the concentrations for all Schmidt numbers Sc were fixed at $c_{Sc}^* = 1$ (indicating fully gas-saturated conditions at all times). Validation of the latter assumption can be found in Duda & Vrentas (1968), who showed that interfacial resistance effects are negligible for atmospheric gases.

To establish fully developed temperature and velocity fields, each simulation was initially run without passive scalar calculations. The velocity field was initially set to zero, while the non-dimensional temperature in (2.4) was initialised by

$$T^*(\zeta^*, t^*) = - \left[2 \sqrt{\frac{t^*}{\pi}} \exp \left(\frac{-(\zeta^*)^2}{4t^*} \right) - \zeta^* \operatorname{erfc} \left(\frac{\zeta^*}{2\sqrt{t^*}} \right) \right], \quad (2.19)$$

where $\zeta^* h = h - z$. The initial simulations started at $t^* = 5.7143 \times 10^{-4}$ at which time random disturbances (uniformly distributed between $T^* = 0$ and 0.0008) were added to the initial temperature field to trigger the RBM instability. The flow was deemed fully developed after it reached a statistically steady state for both the temperature and velocity

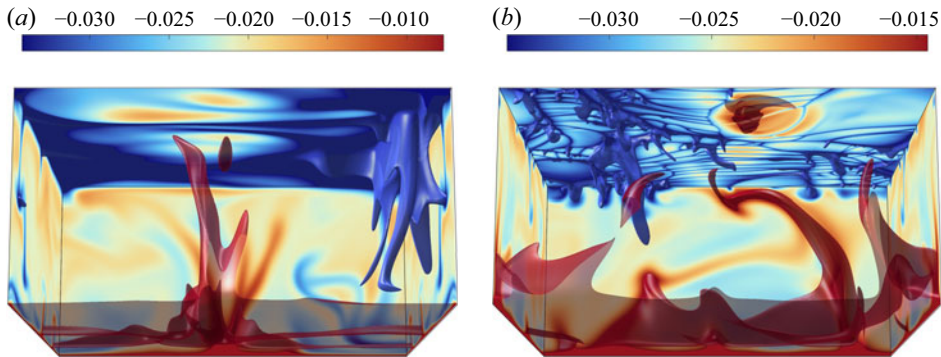


Figure 2. Temperature isosurfaces at $T_1^* = a_{th} \langle T_s^* \rangle_{x,y}$ (blue) and $T_2^* = 2\langle T^*(z = 0.5h) \rangle_{x,y} - T_1^*$ (red) : (a) case $Ma_h = 0$ using $a_{th} = 0.975$, and (b) $Ma_h = 8.81 \times 10^5$ using $a_{th} = 1.175$.

fields. To achieve this, the simulations were run for at least six large eddy-turnaround times corresponding to about $t^* = 0.0114$.

The actual mass transfer simulations were started using the fully developed flow and temperature fields produced in the initial simulations. To quickly establish a quasi-steady turbulent concentration boundary layer, rather than using a zero gas concentration in the interior of the domain, the concentration fields were initialised using the solution of the unsteady diffusion equation (cf. e.g. Fischer *et al.* 1979)

$$c_{Sc}^*(\zeta^*, t^*) = \operatorname{erfc} \left(\zeta^* \sqrt{\frac{Sc/Pr}{4t^*}} \right), \quad (2.20)$$

with $t^* = 5.7143 \times 10^{-4}$. Mass transfer simulations were performed over a period of about three bulk time units, which was deemed to be sufficiently long to obtain statistically quasi-steady results.

3. Results

3.1. Flow topology

Figure 2(a) and 2(b) show snapshots of fully developed temperature fields obtained at $Ma_h = 0$ and 8.81×10^5 , respectively. The figure illustrates the effect of Marangoni forces on the heat exchange mechanism between the cooled water surface and the warmer bottom boundary of the computational domain. Temperature isosurfaces at $T_1^* = a_{th} \langle T_s^* \rangle_{x,y}$ and $T_2^* = 2\langle T^*(z = 0.5h) \rangle_{x,y} - T_1^*$ (where a_{th} is given in the caption) were used to identify, e.g. the thermal plumes that are characteristic for buoyant instabilities. Irrespective of the presence of Marangoni forces, relatively few large buoyant rising plumes of similar size were found to emerge quasi-periodically from the bottom of the computational domain to the surface. While deeply penetrating plumes of similar size and frequency can also be observed to arise from the top in all simulations, their shape and the mechanism by which they form changes with Ma_h . In a fully developed RBM flow, heat fluxes at the surface and bottom of the computational domain need to be in equilibrium. Hence, at $Ma_h = 0$ the shape of these large plumes (that are purely buoyancy-generated) mirrors the situation at the bottom of the domain. Contrastingly, in the presence of Marangoni forces the local near-surface flow topology is significantly affected. For instance, at $Ma_h = 8.81 \times 10^5$ areas containing a multitude of small-scale structures of relatively cold water emerge (cf. figure 2b). Due to the entrainment of these Marangoni generated small-scale

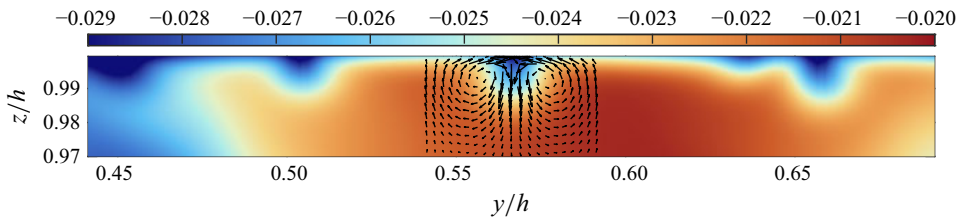


Figure 3. Near-surface cross-sectional temperature distribution with fluctuating velocity vectors to identify counter-rotating vortices at one of the small plumes. The snapshot is from simulation with $Ma_h = 13.21 \times 10^5$ in the plane $x/h = 1$ at $t^* = 0.00295$.

structures, with increasing Ma_h the shape of the large, deeply penetrating plumes becomes more and more irregular. The size of these small-scale structures tends to reduce as they become more numerous with increasing Ma_h . Because of their limited size, the buoyancy force acting on these structures is very small, so that the (horizontally) elongated plume-like structures were found to linger for a significant time at the surface forming a fine, non-uniform mesh.

As illustrated by the detailed cross-section in figure 3, underneath the joint edges of (typically small) neighbouring convection cells, pairs of counter-rotating vortices can be found lying side by side. The Marangoni-induced convection cells form due to surface-temperature gradients, which induce gradients in the surface tension. These gradients generate Marangoni forces that move warm (low surface tension) water along the surface to locations with relatively cool (high surface tension) water. While water moves along the surface it is gradually cooled due to evaporation. At the edges of convection cells, opposing streams of cooled water collide, generating small plumes of cold water that are actively pushed down into the upper bulk by the surface Marangoni forces. A more quantitative discussion of the Marangoni plumes will be presented in § 3.5.

The Marangoni effect on the near-surface flow topology is elucidated in figure 4, showing sequences of surface divergence ($\beta^* = -\partial w^*/\partial z^*$) contour plots for cases M0, M1, M5, M10 and M15 (cf. table 1). A non-uniform distribution of large and small convection cells can already be observed at $Ma_h = 0.88 \times 10^5$ (case M1). The average proportion of the surface occupied by small cells is observed to increase significantly with Ma_h (which is further quantitatively evidenced by the histograms in figure 5). As a result, on average the number of large cells becomes negligible (even though the area they occupy remains non-negligible) compared to the number of small convection cells. Obviously, as the number of cells increases, the characteristic length scale of the small cells tends to gradually reduce with Ma_h , which is in agreement with the dimensional analysis (2.13), as was previously reported by, e.g. Schwarzenberger *et al.* (2014). Note that to compute the area of individual convection cells, the cells were identified by isolated patches at the surface with a surface divergence $\beta^* \geq -0.5\beta_{rms}^{*-}$, where β_{rms}^{*-} is the corresponding root mean square of all $\beta^* \leq 0$.

From the sequences in figure 4, it can also be seen that, for $Ma_h \geq 4.4 \times 10^5$, the number of small cells (and, hence, the surface area that they occupy) significantly fluctuates in time between two limiting states, one with relatively few cells and one with a large number of cells. The time interval between the two limiting states is determined by the characteristic period at which large plumes are generated by buoyancy forces at the bottom of the computational domain. Starting from the state with a relatively large number of (small) convection cells (roll cells), a (significant) reduction in the number of these cells is achieved through the surface interaction between warm buoyant plumes and Marangoni structures. On their way to the surface (depending on the strength of the

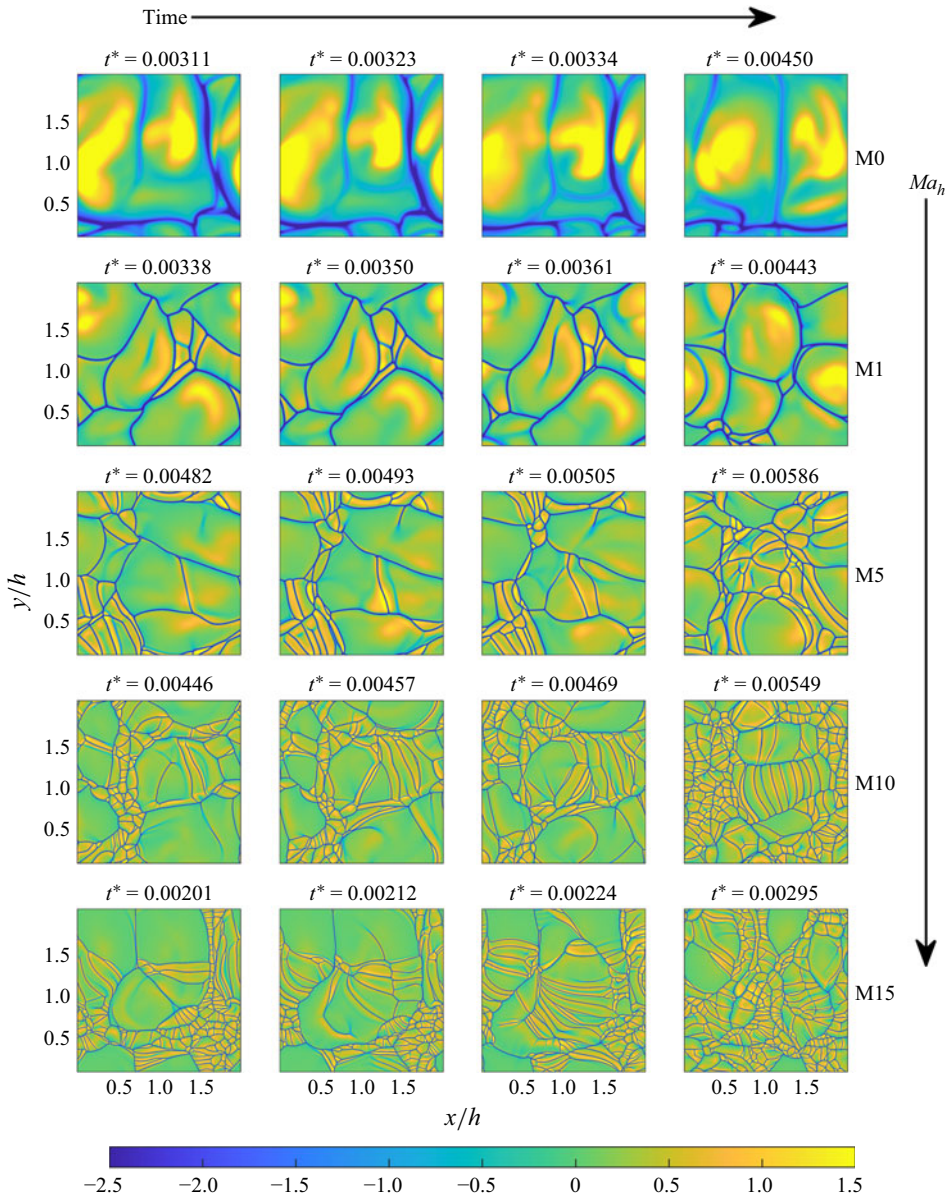


Figure 4. Sequences of scaled surface divergence β^*/β_{rms}^* contour plots extracted from cases M0, M1, M5, M10 and M15 with $[Ma_h; \beta_{rms}^*] = [0; 0.44 \times 10^4], [0.88 \times 10^5; 0.80 \times 10^4], [4.40 \times 10^5; 2.71 \times 10^4], [8.81 \times 10^5; 6.51 \times 10^4], [13.21 \times 10^5; 9.4 \times 10^4]$, respectively. The first image in each row represents a snapshot near the end of a large-rising-plume event, characterised by an overall reduction in the number of cells and often by large regions completely devoid of small-scale Marangoni structures. The two subsequent images show the emergence of small-scale Marangoni plumes in the absence of large-plume events. In each row, the time interval between the first, second and third snapshots is $\Delta t^* = 0.000115$. The last snapshot is about 0.5 bulk time units apart from the first snapshot and illustrates the state immediately before the next large-plume event (see § 3.2 for the increase in β_{rms}^* with Ma_h).

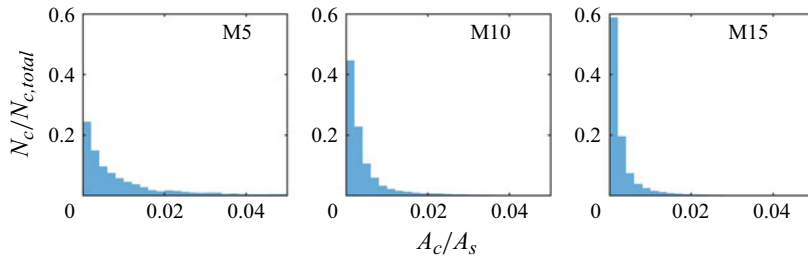


Figure 5. Distribution of convection cell footprint sizes from cases M5, M10 and M15 with $Ma_h = 4.40 \times 10^5$, 8.81×10^5 and 13.21×10^5 , respectively. Here A_c/A_s is the proportion of surface area occupied by a convection cell.

plumes) the displaced water generated by these plumes either (i) sweeps near-surface structures immediately above to the side, resulting in rapidly spreading large convection cells, similar to the eruptions reported in Köllner *et al.* (2016) that are completely devoid of any small-scale Marangoni structures (cf. left most panes in figure 4), or (ii) gets entrained into the Marangoni cells, thereby (significantly) increasing their size (small eruptions). Both events result in an overall reduction of the number of cells.

After such reduction events, there is usually a period with no or very minor interactions between warm buoyant plumes and near-surface structures. During such periods the number of small cells quite rapidly increases due to a sequence of Marangoni-induced cell divisions. A possible explanation of the cell division process is provided below. It starts with pairs of counter-rotating vorticities lying side by side along opposite edges of the convection cell. Each vortex has a footprint consisting of a narrow strip of negative surface divergence at the joint edge of neighbouring (often) elongated convection cells, which are typically sandwiched between narrow areas of high positive surface divergence (cf. figure 4). If the cell is sufficiently large, these vortices will induce a pair of counter-rotating mirror vorticities (transporting fluid from the surface into the upper bulk). As these mirror vorticities become stronger, this process will eventually lead to the break up of the convection cell into smaller cells.

Below, the aforementioned observations will be further analysed and linked to the interfacial heat and mass transfer.

3.2. Flow statistics

Figures 6(a) and 6(b) show profiles of the normalised velocity fluctuations ($\sqrt{\langle w'w' \rangle}/U_\kappa$, $\sqrt{\langle u'u' + v'v' \rangle}/(2U_\kappa)$) as a function of z/h , where $\langle \cdot \rangle$ denotes averaging both in time and the (homogeneous) horizontal directions. The profiles shown are characteristic also for the other simulations, and illustrate that, irrespective of the Marangoni number, the vertical fluctuations in the bulk are roughly 1.5 to 2.5 times larger than the horizontal fluctuations. This indicates that the momentum transport in the bulk is predominantly in the vertical direction, which is due to the rising and sinking buoyant plumes (see also figure 2). The typical non-dimensional time scale for the large-scale fluctuations in the bulk – driven mostly by buoyancy – as estimated by

$$\tau_b^* = \tau_b U_\kappa / h = \frac{\kappa}{\int_0^z \sqrt{\langle w'w' \rangle} dz} \quad (3.1)$$

was found to be about 0.002093 in all simulations and, therefore, appears to not depend on Ma_h .

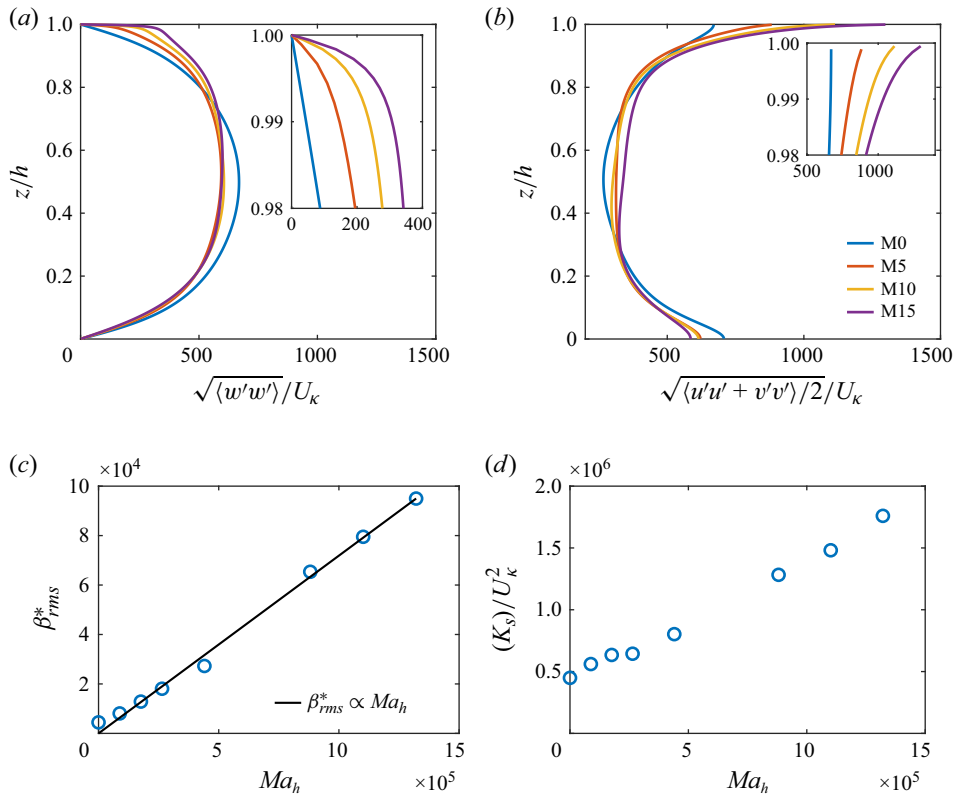


Figure 6. Flow statistics: (a) vertical velocity fluctuations and (b) horizontal velocity fluctuations as a function of z/h extracted from simulations M0, M5, M10, M15, with $Ma_h = 0, 4.40 \times 10^5, 8.81 \times 10^5$ and 13.21×10^5 , respectively. (c) Variation of surface divergence β_{rms}^* and (d) surface kinetic energy K_s as a function of Ma_h .

Figures 6(a) and 6(b) also show the significant enhancement in both the horizontal and vertical velocity fluctuations immediately below the surface with increasing Ma_h . These enhanced fluctuations are only able to penetrate thin layers adjacent to the surface (before the profiles intersect with the $Ma_h = 0$ profile). The thickness of these layers was found to be roughly $0.1h$ and $0.2h$ for the horizontal and vertical fluctuations, respectively. Further down, the flow is dominated by buoyancy.

The significant increase in the velocity fluctuations just below the surface is a direct consequence of the boundary condition (2.9): at the surface, the gradients in the horizontal fluctuations depend linearly on Ma_h . Hence, for Marangoni-dominated flows, with increasing Ma_h , the surface divergence ($\beta^* = -\partial w^* / \partial z^* = \partial u^* / \partial x^* + \partial v^* / \partial y^*$) also increases linearly with Ma_h , which is evidenced in figure 6(c). As a result, the magnitude of the downward velocity of the Marangoni plumes at the surface increases, which is in agreement with (2.14). Note that while β increases with Ma_h for surface-temperature-gradient-induced Marangoni forces, it decreases with increasing Marangoni number for surfactant-induced Marangoni forces. A detailed explanation of the physical mechanisms involved in the latter can be found in, e.g. Shen, Yue & Triantafyllou (2004), McKenna & McGillis (2004), Wissink *et al.* (2017). The effects of these different mechanisms on interfacial mass transfer will be discussed in § 3.6.

In Wissink & Herlina (2023) it was shown that for the developing purely Marangoni driven instability, the total surface kinetic energy $\langle K_s \rangle$ linearly depends on the Marangoni

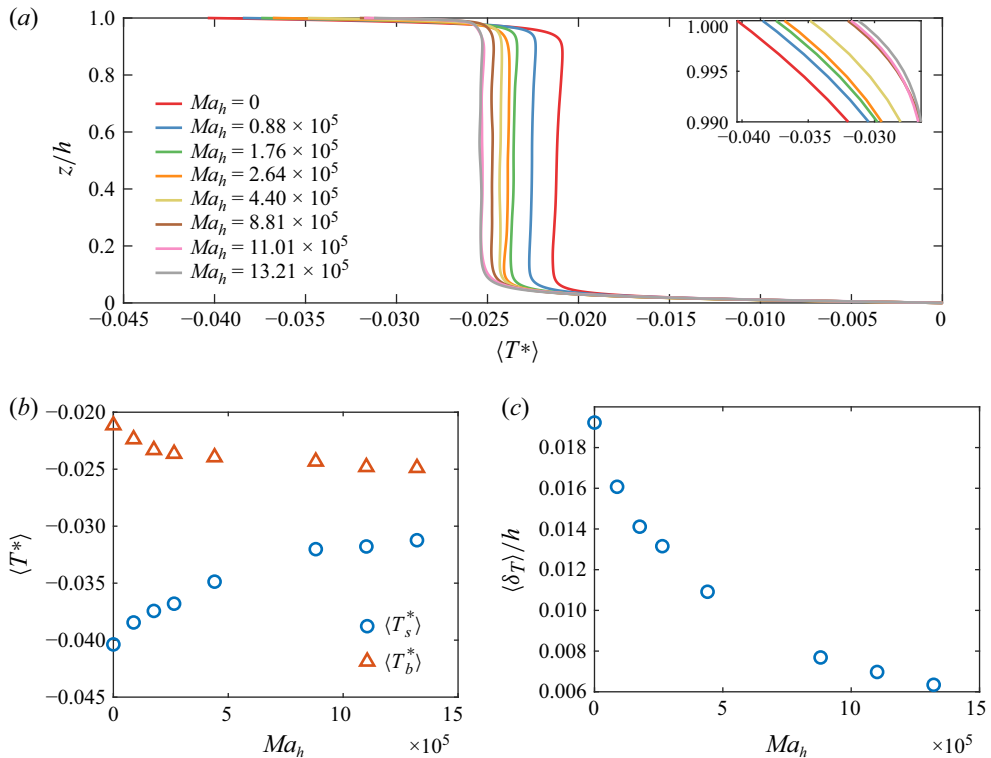


Figure 7. (a) Normalised temperature profiles at various Marangoni numbers. (b) Variation of normalised surface temperature and bulk temperature as a function of Ma_h . (c) Non-dimensional mean thermal boundary layer thickness $\langle \delta_T \rangle / h$.

number. When adding buoyancy (RBM instability), this linear dependency only persisted at sufficiently large Marangoni numbers. Similarly, also for fully developed RBM instabilities (with constant Ra_h), a clear linear dependency of $\langle K_s \rangle$ on Ma_h was only found for larger Ma_h (cf. figure 6d). For smaller Ma_h , buoyancy becomes increasingly important resulting in a gradual loss of linearity.

3.3. Mean temperature profile and heat transfer scaling

Figure 7(a) shows time and horizontally averaged temperature profiles. All profiles are characterised by relatively thin thermal boundary layers at the surface and bottom, and have an extended constant (fully mixed) temperature region in the bulk. When increasing the Marangoni force, the surface temperature $\langle T_s^* \rangle$ can be seen to become warmer due to a more intense vertical mixing near the surface. Simultaneously, because of the increased transfer rate of relatively cold surface water into the bulk, the bulk temperature $\langle T_b^* \rangle$ becomes colder, and approaches an asymptotic value of about -0.025 (cf. figure 7b). As can be seen in figure 7(c), this increased vertical mixing at the surface results in a thinning of the mean surface thermal boundary layer thickness $\langle \delta_T \rangle$ defined in (2.11).

Figure 8(a) shows the corresponding non-dimensional heat transfer velocity (Nusselt number), defined as

$$Nu = \frac{qh}{\langle T_s - T_b \rangle} = \frac{h}{\langle \delta_T \rangle}, \quad (3.2)$$

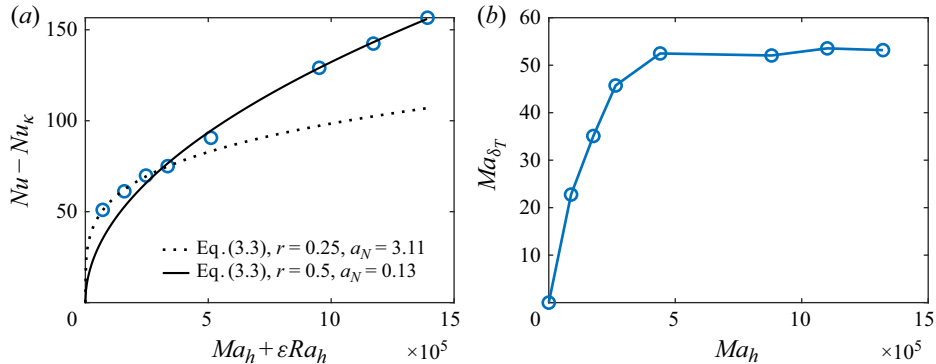


Figure 8. (a) Variation of non-dimensional heat transfer velocity $Nu - Nu_\kappa$ as a function of $Ma_h + \varepsilon Ra_h$, with $\varepsilon = 0.0016$. (b) Variation of Ma_{δ_T} with Ma_h .

as a function of $(Ma_h + \varepsilon Ra_h)$ rather than Ma_h to reflect the fact that the Marangoni and buoyant instabilities reinforce one another (cf. e.g. Nield 1964). At first sight, the data suggest a linear relation between Nu and $(Ma_h + \varepsilon Ra_h)$. However, for $q \leq 0$, it is to be expected that $\delta_T \rightarrow h$ due to thermal diffusion when $Ma_h, Ra_h \rightarrow 0$, so that $Nu \rightarrow Nu_\kappa = 1$, where Nu_κ is the Nusselt number corresponding to the purely diffusive case. The latter is not predicted by a linear interpolation so that a power law relation,

$$(Nu - Nu_\kappa) = a_N (Ma_h + \varepsilon Ra_h)^r, \quad (3.3)$$

is more applicable. Note that $\varepsilon = 0.0016$ and a_N (cf. figure 8a) were determined empirically. In fact, the figure suggests the existence of two regimes. For the buoyancy-dominated regime, Ma_h can be seen to modulate the Rayleigh number, effectively replacing $(Ma_h + \varepsilon Ra_h)$ by Ra_{eff} . The obtained value of $r = 0.25$ is consistent with the *a priori* estimate $\delta_R \propto \delta_T \propto Ra_{eff}^{-0.25}$ for purely buoyancy-driven flows (cf. § 2.2). Similarly, in the Marangoni-dominated regime, Ra_h slightly alters Ma_h , so that an effective Marangoni number $Ma_{eff} = (Ma_h + \varepsilon Ra_h)$ is obtained. Here, the value of $r = 0.5$ was found to provide a very good interpolation of the data and is consistent with the *a priori* scaling $\delta_\sigma \propto \delta_T \propto Ma_{eff}^{-0.5}$ for purely Marangoni driven flows (cf. § 2.2). The existence of such a Marangoni-dominated regime is further evidenced in figure 8(b), where for $Ma_h \geq 4.4 \times 10^5$, $Ma_{\delta_T} = Ma_h (\delta_T / h)^2$ becomes approximately constant converging to a value of about 53. Note that the existence of such a dual regime (Rayleigh-dominated vs Marangoni-dominated) was also found in the developing RBM instability case (Wissink & Herlina 2023). Furthermore, to facilitate comparison with experiments and other simulations, it could be convenient to recast the $Ma_h + \varepsilon Ra_h$ into $Bo_h^{-1} + \varepsilon$, where $Bo_h = Ra_h / Ma_h$ is the Bond number.

3.4. Temperature fluctuations

As observed in figure 9(a), due to the action of Marangoni forces at the surface, significant differences in the $T_{rms}^* = \sqrt{\langle T^* T^* \rangle}$ profiles can be seen in the upper bulk. These differences gradually decrease with distance to the surface, though their presence is still noticeable near $z = 0$. The temperature fluctuation at the surface, $T_{rms,s}^*$, and the peak in T_{rms}^* near the surface both become smaller with increasing Ma_h . This is associated with the variation of the temperature gradient $|\langle \partial T^* / \partial z^* \rangle|$ with z/h shown in figure 9(b), where the locations of the T_{rms}^* peaks are indicated by the red crosses. It can be seen that for $Ma_h \leq 1.76 \times 10^5$, the location of these peaks is fully embedded in a region of relatively

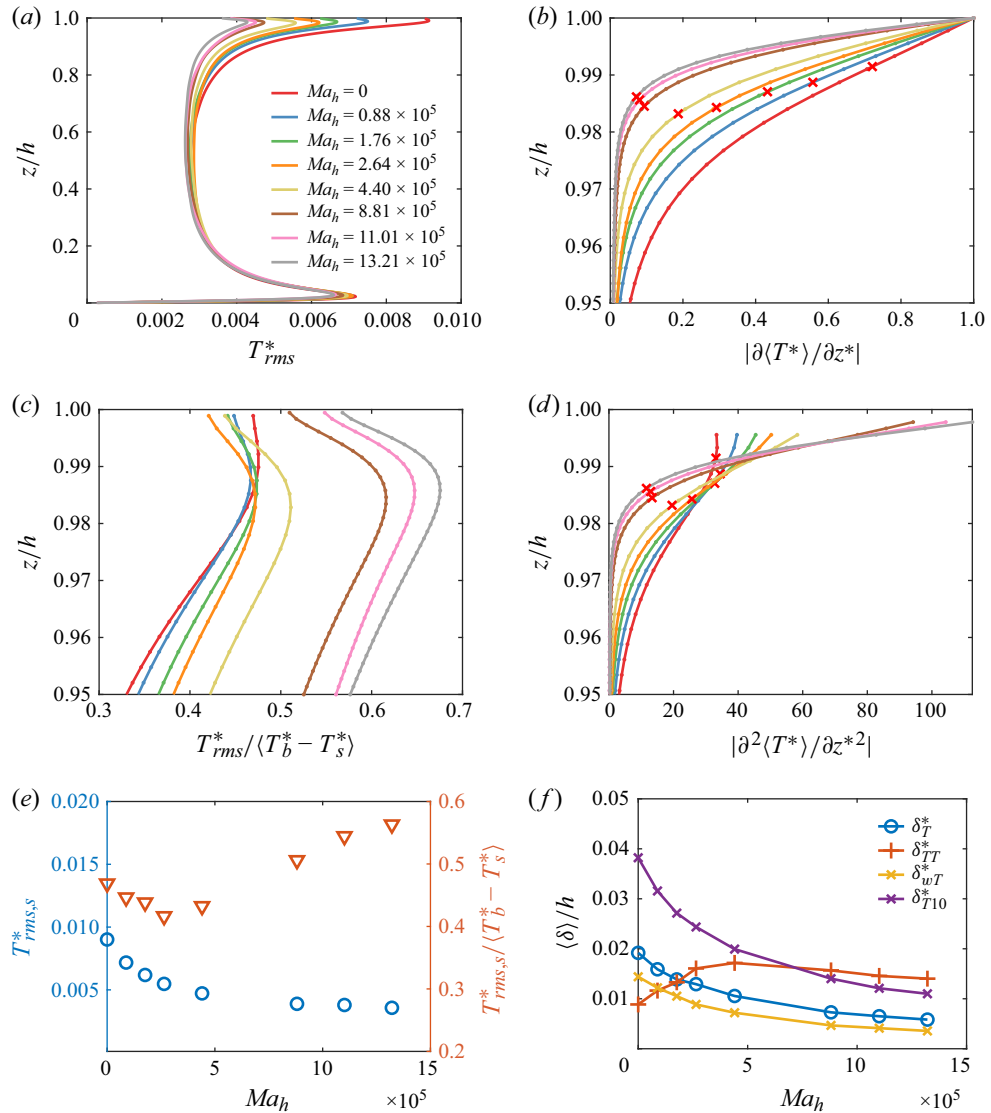


Figure 9. Profiles at various Marangoni numbers of (a) normalised temperature fluctuation, (b) normalised temperature gradient $|\partial \langle T^* \rangle / \partial z^*|$, (c) $T_{rms}^* / (T_b^* - T_s^*)$, (d) $|\partial^2 \langle T^* \rangle / \partial z^{*2}|$. Variation of (e) surface-temperature fluctuations and (f) boundary layer thickness with Ma_h .

large $|\langle \partial T^* / \partial z^* \rangle|$ and, therefore, associated with a relatively large production of T_{rms}^* . In contrast, for $Ma_h \geq 8.81 \times 10^5$, the peak in T_{rms}^* is located in a region of relatively small $|\langle \partial T^* / \partial z^* \rangle|$ leading to a much reduced production of T_{rms}^* .

To explain the latter, in figure 9(c), T_{rms}^* is scaled by $\langle T_b^* - T_s^* \rangle$ to remove any bias due to the Ma_h dependency of $\langle T_b^* - T_s^* \rangle$. It can be seen that at the surface the scaled temperature fluctuation $\theta' = T_{rms,s}^* / (T_b^* - T_s^*)$ only slightly reduces with increasing Ma_h for $Ma_h \leq 2.65 \times 10^5$. Contrastingly, θ' values were found to increase with Ma_h for larger Marangoni numbers (cf. also figure 9e). The latter indicates a major change in the surface flow dynamics as the RBM instability becomes dominated by Marangoni forces.

Furthermore, it can be observed that below the surface both θ' and the relative size of the peaks $\theta'_p - \theta'_s$ (where the subscripts p, s correspond to the peak and surface, respectively) tend to increase with Marangoni number (cf. figure 9c). This increase is closely linked to the decay rate of vertical temperature gradients expressed by $|\langle \partial^2 T^* / \partial z^*{}^2 \rangle|$ shown in figure 9(d). At $Ma_h = 0$, this decay is slowest and results in a relatively small peak in θ' located very close to the surface. The increase in the decay of the gradient $|\langle \partial T^* / \partial z^* \rangle|$ with increasing Ma_h results in an enhanced increase in θ' with distance to the surface, leading to an increase in $\theta'_p - \theta'_s$ and an approximately linear increase in the thickness δ_{TT}^* (which is the distance between the location of θ'_p – identified by the markers in figure 9d – and the surface), at least for $Ma_h \leq 4.4 \times 10^5$.

For the larger Marangoni numbers $Ma_h \geq 8.81 \times 10^5$, the very rapid decrease in the gradient $|\langle \partial T^* / \partial z^* \rangle|$ in the near-surface region still leads to a further increase in $\theta'_p - \theta'_s$. Simultaneously the location where the gradient becomes too weak to support any further growth in θ' approaches the surface, eventually resulting in a reduction in δ_{TT}^* . Note that the latter mechanism already affects the results at $Ma_h = 4.4 \times 10^5$, which can also be seen in figure 9(f), where δ_{TT}^* exhibits linear growth only for the smaller $Ma_h \leq 2.64 \times 10^5$, while for larger Ma_h , this trend reverses. For comparison, also included in figure 9(f) are δ_T^* , δ_{wT}^* (the distance between the peak in the $\langle w^* T^* \rangle$ profile and the surface) and finally δ_{T10}^* , which is defined as the distance between the surface and the location where $|\partial \langle T^* \rangle / \partial z^*| = 0.1 |\partial T^* / \partial z^*|_s$. It can be seen that for $Ma_h \leq 2.64 \times 10^5$, δ_{TT}^* is significantly smaller than δ_{T10}^* , indicating a non-negligible vertical gradient in T for $0 \leq \zeta \leq \delta_{T10}^*$, while for $Ma_h \geq 8.81 \times 10^5$, δ_{TT}^* was found to be slightly larger than δ_{T10}^* .

The above statistics can be linked to the flow dynamics discussed earlier in § 3.1 (cf. figures 2 to 4). Because of the very few (large) plumes emerging at $Ma_h = 0$, the location of the peak in the horizontal temperature fluctuations is relatively close to the surface. For the smaller $Ma_h \leq 4.40 \times 10^5$, the number of plumes somewhat increases with Ma_h causing the T_{rms}^* peak to move further away from the surface. This trend is reversed for the larger Marangoni numbers, where the average convection cell size significantly reduces and, hence, the size of the plumes formed at the edges of these cells becomes very small. Consequently, these small plumes lose buoyancy and tend to linger immediately under the surface for a significant time until either the larger of these plumes become sufficiently buoyant and moves into the upper bulk, or a significant buoyant event from below displaces these small convection cells, dragging them into the bulk. As a result, the T_{rms}^* peak approaches the surface with increasing $Ma_h \geq 8.81 \times 10^5$.

3.5. Concentration profiles and Marangoni layer

As mentioned in § 2.4, after the fully developed flow and temperature fields were established, mass transfer calculations for four different Schmidt numbers ($Sc = 16, 50, 100, 200$) were activated starting with the initial concentration profiles given in (2.20). In all simulations, a statistically quasi-steady state for the mass concentrations was achieved within one bulk time unit.

Figure 10(a) shows (passive) scalar concentration profiles at $Sc = 200$. The shape of the mean profiles can be seen to significantly change with increasing Marangoni number. As typical for a buoyancy-dominated flow, at $Ma_h = 0$ the profile shows a gradual decrease in concentration when moving away from the surface. Contrastingly, for $Ma_h \geq 4.40 \times 10^5$, the profiles are characterised by the appearance of a local minimum in the concentration very close to the surface. This minimum is followed by a local maximum, indicating the approximate location of the edge of the relatively thin Marangoni layer.

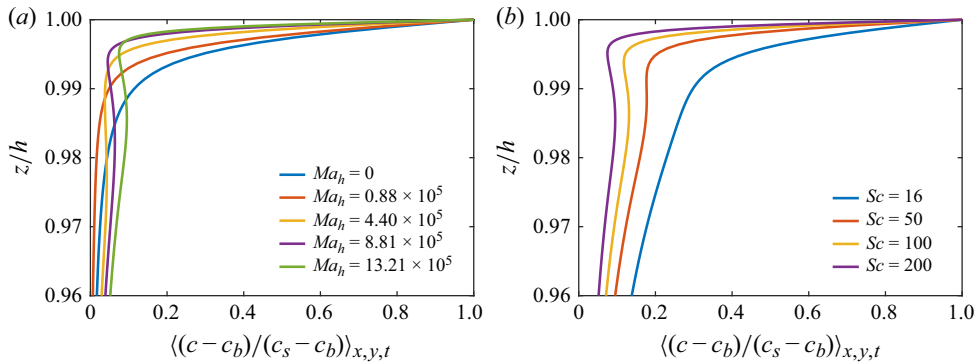


Figure 10. Near-surface concentration profiles (a) for various Ma_h at $Sc = 200$, (b) for various Sc at $Ma_h = 13.2 \times 10^5$ (case M15).

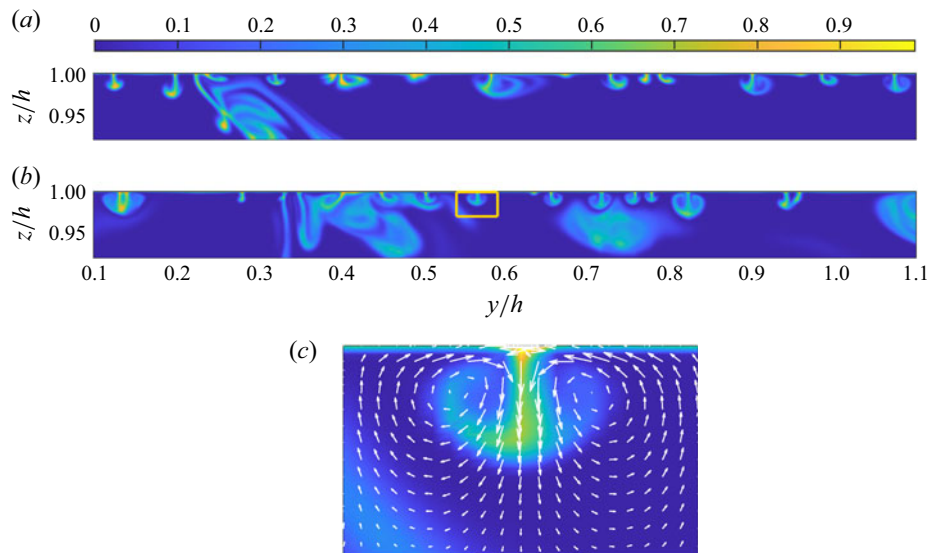


Figure 11. Near-surface cross-sectional concentration distribution for $Sc = 200$ and $Ma_h = 13.21 \times 10^5$ in the plane $x/h = 1$ at (a) $t^* = 0.00224$, (b) $t^* = 0.00295$. (c) Detailed view of the Marangoni plume identified by the box in (b), together with fluctuating velocity vectors.

An explanation of these features can be seen in figure 11, showing cross-sectional snapshots at $x/h = 1$ of the concentration at $Sc = 200$ focusing on the near-surface region of simulation M15 ($Ma_h = 13.21 \times 10^5$). The snapshots shown were extracted at $t^* = 0.00224$ (figure 11a) and $t^* = 0.00295$ (figure 11b). The corresponding convection cell footprints at the surface can be found in figure 4. Both snapshots show a multitude of plumes of varying sizes. Most of the plumes are small with a limited penetration depth and are associated with the small convection cells observed in figure 4 that are typical for Marangoni-dominated flows. Figure 11(c) shows a detailed cross-section through the Marangoni plume identified by the rectangle in figure 11(b), together with fluctuating velocity vectors. As illustrated in the figure, because of the specific topology of this characteristic Marangoni plume, which is connected to the surface by its stalk, a clearly identifiable minimum in concentration is obtained between the surface and the lobes of the

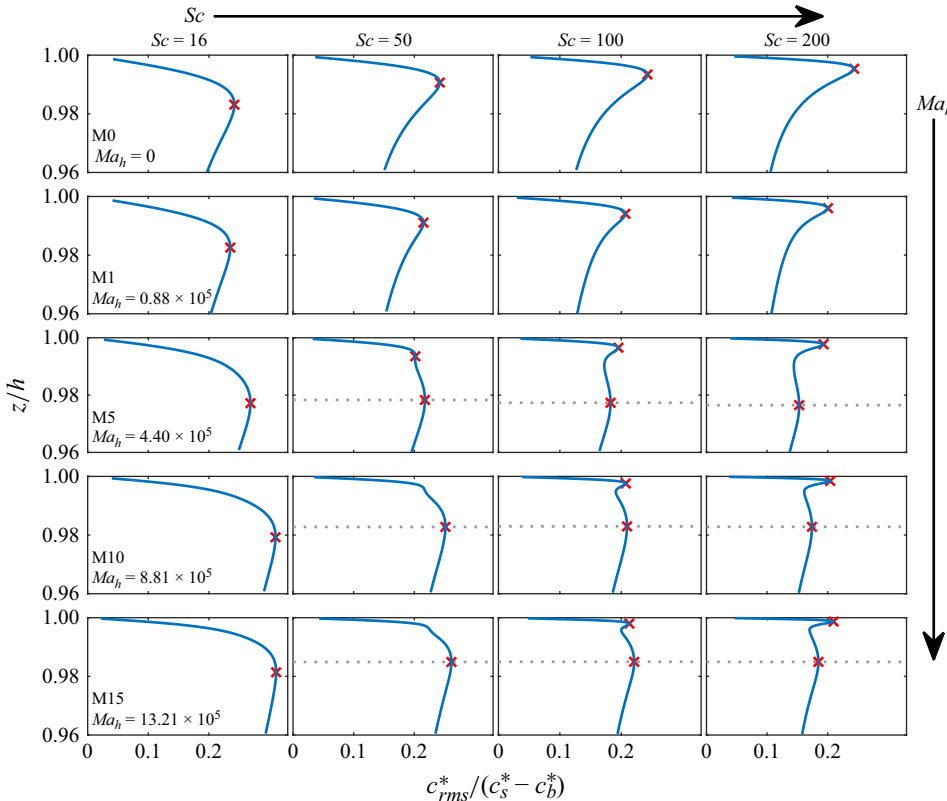


Figure 12. Profiles of the normalised concentration fluctuations $c_{rms}^*/(c_s^* - c_b^*)$ for $Sc = 16 - 200$ as obtained in simulations M0, M1, M5, M10, M15.

plume. The Marangoni plume typically starts its life as a downward moving jet of cold, saturated flow that induces two counter-rotating surface-parallel vortices on either side of its symmetry plane (cf. also figure 3). As it approaches its maximum penetration depth, the two vortices move warm, unsaturated ambient water upwards around the lobes and finally inwards immediately below the surface. This process is responsible for the appearance of a local minimum in the mean near-surface concentration profile.

The presence of the Marangoni sublayers in the mean concentration profiles at $Sc = 200$ and $Ma_h \geq 4.40 \times 10^5$ are visible owing to the combination of very low scalar diffusivity and a sufficiently high Marangoni number, which ensures that scalar diffusivity and buoyancy effects, respectively, do not mask the characteristic features of the Marangoni-dominated region in the concentration profiles. In contrast, as depicted in figure 10(b) (showing the mean concentration profiles obtained at $Ma_h = 13.21 \times 10^5$ for $Sc = 16, 50, 100, 200$), the local minima in the profiles that are located very close to the surface gradually vanish as the diffusivity increases with reducing Schmidt number. Figures 10(a) and 10(b) also clearly show the (expected) significant reduction in the concentration boundary layer thickness (steepening of the concentration gradient $(\partial c^*/\partial z^*)$ at the surface) both with increasing Ma_h and Sc . The former due to stronger fluctuations introduced to the upper bulk by the Marangoni forces and the latter by reduced scalar diffusivity.

In figure 12 the effect of increasing Ma_h and Sc on the concentration fluctuation ($c_{rms}^* = \sqrt{\langle c'^* c'^* \rangle}$) profile is shown. A significant difference can be observed between the profiles

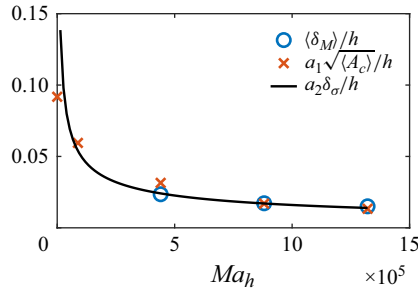


Figure 13. Variation of the Marangoni layer thickness $\langle \delta_M \rangle / h$ with Ma_h . For comparison, also shown are the estimates $\langle \delta_M \rangle / h \approx a_1 \sqrt{A_c} / h$ and $\langle \delta_M \rangle / h \approx a_2 \delta_\sigma / h \propto Ma_h^{-0.5}$, with $a_1 = 0.1$ and $a_2 = 1.6$. Here $\langle A_c \rangle$ denotes the approximate convection cell footprint area and δ_σ is the *a priori* estimate of the Marangoni layer (2.13).

of the two most extreme cases studied here (M0 with $Ma_h = 0$, $Sc = 16$ versus M15 with $Ma_h = 13.21 \times 10^5$, $Sc = 200$). While in the former case, only one peak near the surface is observed, two peaks can be clearly identified in the latter case. The distinct characteristics of these profiles for the different regimes are discussed in more detail below.

For cases M0 and M1 ($Ma_h \leq 0.88 \times 10^5$), the c_{rms}^* profiles show a well-defined maximum (identified by 'x'). The distance between this (local) maximum and the surface corresponds to the concentration boundary layer thickness $\langle \delta_c \rangle / h$, which is found to gradually decrease with increasing Schmidt number.

For cases M5–M15 ($Ma_h \geq 4.40 \times 10^5$) and $Sc \geq 100$, two well-defined c_{rms}^* peaks were observed. The surface-nearest peak was found to coincide with the edge of the concentration boundary layer, of which the thickness

$$\frac{\langle \delta_c \rangle}{h} = \left| \frac{c_s^* - c_b^*}{\partial c^* / \partial z^*|_s} \right| \quad (3.4)$$

can be seen to reduce with increasing Sc . The thickness, δ_M , of the Marangoni layer is defined by the distance between the surface and the penetration depth of the Marangoni plumes. It was found that δ_M approximately corresponds to the distance between the surface and the location of the lower peak (identified by the dashed grey line). The figure clearly shows that this location only depends on Ma_h and is Sc independent. Note that for the cases M5–M15, the c_{rms}^* profiles at $Sc = 50$ already suggest the presence of two peaks of which the lower one coincides with the dashed grey line.

Figure 13 shows that the thickness of the Marangoni layer $\langle \delta_M \rangle$ decreases with increasing Ma_h according to the power law $\langle \delta_M \rangle \propto Ma_h^{-0.5}$, which is in agreement with the *a priori* determined scaling of the Marangoni length scale δ_σ (2.13). Also shown is an estimate of $\langle \delta_M \rangle$ using $\langle \delta_M / h \rangle \approx 0.1 \sqrt{A_c} / h$, where A_c is the approximate convection cell footprint area. For the larger Marangoni numbers, this estimate provides a reasonably good prediction of the Marangoni layer thickness, confirming the close relation between the characteristic Marangoni convection cell footprint and the thickness of the Marangoni layer.

3.6. Scaling of mass transfer velocity

Previously it was shown that due to increased mixing near the surface, the non-dimensional heat transfer, expressed by the Nusselt number, significantly increases with Marangoni number. The same is expected for the mass transfer velocity

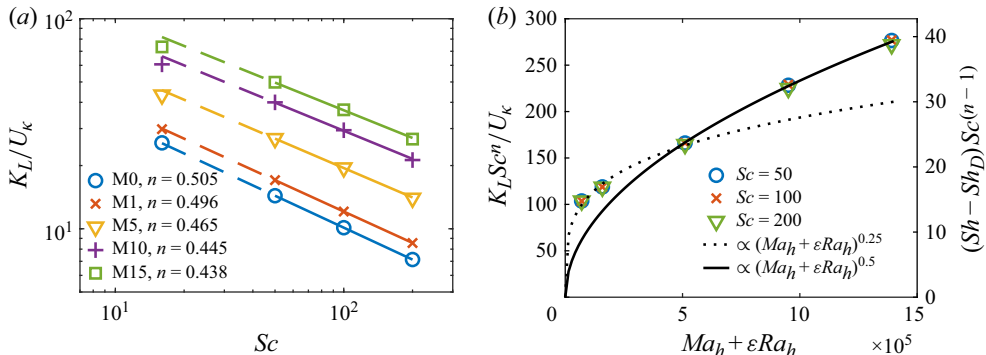


Figure 14. (a) Scaling of the normalised transfer velocity $K_L/U_k \propto Sc^{-n}$ for cases M0, M1, M5, M10, M15, with $Ma_h = 0, 0.88 \times 10^5, 4.40 \times 10^5, 8.81 \times 10^5$ and 13.21×10^5 , respectively. The obtained values for n are based on the higher $Sc \geq 50$ cases, indicated by the solid lines. (b) Variation of the normalised transfer velocity K_L and Sh as a function of $(Ma_h + \varepsilon Ra_h)$. The solid line represents $K_L Sc^n/U_k = 0.23(Ma_h + \varepsilon Ra_h)^{0.5}$ and $(Sh - Sh_D) Sc^{n-1} = 0.033(Ma_h + \varepsilon Ra_h)^{0.5}$, while the dashed line represents $K_L Sc^n/U_k = 6.12(Ma_h + \varepsilon Ra_h)^{0.25}$ and $(Sh - Sh_D) Sc^{n-1} = 0.88(Ma_h + \varepsilon Ra_h)^{0.25}$, where $\varepsilon = 0.0016$ and n can be found in the legend of (a).

$$k_L = \frac{-D \partial c / \partial z|_s}{c_s - c_b} \quad (3.5)$$

of the passive scalars, representing atmospheric gases. This expected increase in $K_L = \langle k_L \rangle$ is in stark contrast to what was observed at contaminated surfaces, where the surfactant-concentration-gradient-induced Marangoni forces tend to inhibit mass transfer. In Wissink *et al.* (2017) it was shown that n in $K_L \propto Sc^{-n}$ gradually decreases from $n = 0.667$ for severely contaminated surfaces to $n = 0.5$ for surfactant-free surfaces. In the current simulations, the power n (obtained using the results for $Sc \geq 50$) was found to continuously reduce further with increasing Marangoni number from $n \approx 0.5$ at $Ma_h = 0$ to $n \approx 0.438$ at $Ma_h = 13.2 \times 10^5$ (see figure 14a). This reduction in n confirms the promotion of interfacial mass transfer by surface-temperature-gradient-induced Marangoni forces to values clearly below $n = 0.5$. The results presented make it likely that even lower values of n are possible for $Ma_h > 13.2 \times 10^5$. In addition, at each Ma_h the unique scaling of K_L with Sc (shown in figure 14a) for $Sc \geq 50$ can likely be extrapolated to $Sc > 200$, as supported by previous DNS results performed for Sc up to 500 (e.g. Herlina & Wissink 2014; Wissink & Herlina 2016; Herlina & Wissink 2019).

This overall trend can be explained using the eddy diffusivity model of Ledwell (1984) that reads

$$K_L \approx \left(\int_0^\infty [D + D_1]^{-1} d\xi \right)^{-1}, \quad (3.6)$$

and is valid for D sufficiently small. Here, the eddy diffusivity D_1 is modelled by the product of the mixing length $L(\xi) \approx \xi$ (distance to the surface) and the mixing velocity $w_{rms}(\xi)$ (the root mean square of the vertical velocity) evaluated near the surface, which is responsible for the vertical transport of mass. By subsequently approximating the behaviour of $w_{rms}(\xi)$ immediately below the surface using $w_{rms}(\xi) \approx a\xi^\gamma$ (where a is a constant), the eddy diffusivity

$$D_1(\xi) \approx a\xi^{1+\gamma} \quad (3.7)$$

is obtained. For free-slip and no-slip boundary conditions, $\gamma = 1$ and $\gamma = 2$, respectively, can be obtained analytically using a Taylor series expansion of w' near the surface.

Employing these values of γ in (3.6) leads to the scaling $K_L \propto D^n$ (equivalent to $K_L \propto Sc^{-n}$), where $n = 1/2$ for free-slip and $n = 2/3$ for no-slip boundary conditions (as shown in Ledwell (1984)). As mentioned above, Wissink *et al.* (2017) found a smooth transition between these two states with increasing surface pollution. Following this approach, this smooth transition can be retrieved using $1 \leq \gamma \leq 2$ in (3.7). Similarly, in the present simulations, eddy diffusivities D_1 obtained for positive $\gamma \leq 1$ can be employed to predict the observed gradual changes in n (cf. figure 14a). Overall, by combining all results, the present data suggest that n increases from ≈ 0.438 at $Ma_h = 13.2 \times 10^5$ to $n = 0.5$ at $Ma_h = 0$, while a further increase to $n = 0.667$ is obtained in the study of surfactant-induced Marangoni forces. Note that in the latter case the transport of surfactant-free (high surface tension) bulk water to the surface is counteracted by surfactant-gradient-induced Marangoni forces. This is opposite to what is happening in our present simulations, where the transport of relatively warm (low surface tension) bulk water is promoted by surface-temperature-gradient-induced Marangoni forces.

Figure 14(a) also shows that for constant Sc , the transfer velocity increases with Ma_h . This increase correlates with the steepening of the corresponding surface concentration gradients at $Sc = 200$ (and the thinning of the concentration boundary layer) with increasing Ma_h , shown in figure 10(a). This enhancement is also illustrated in figure 14(b), which shows the equivalent power law relations

$$K_L Sc^n / U_\kappa = a_K (Ma_h + \varepsilon Ra_h)^r \quad (3.8)$$

and

$$(Sh - Sh_D) Sc^{n-1} = a_S (Ma_h + \varepsilon Ra_h)^r, \quad (3.9)$$

where $Sh = K_L h / D$ is the Sherwood number, $Sh_D = 1$ is the Sherwood number for the purely diffusive case, n is displayed in figure 14(a), a_K , a_S are the coefficients of proportionality (cf. caption of figure 14b) and, as in (3.3), $r = 0.25$ in the buoyancy-dominated regime, $r = 0.5$ in the Marangoni-dominated regime and $\varepsilon = 0.0016$. Using this scaled transfer velocity the data points for various Schmidt numbers can be seen to collapse and evidence is provided of the existence of the two regimes. Note that because of the extremely expensive computational cost, the (high) Schmidt number mass transfer statistics were gathered over a time interval of only two bulk time units and only for a selection of Ma_h (cf. table 1), while heat transfer statistics were gathered for all Ma_h over time intervals exceeding 10 bulk time units. Despite the fewer data points, the evidence for a buoyancy-dominated regime in the mass transfer case is still quite clear.

3.7. Surface structures and quantities

As can be seen in figure 5, due to the strength of the Marangoni forces at $Ma_h \geq 4.40 \times 10^5$, the vast majority of convection cells is very small compared to the surface area of the computational domain. Only a few large cells (induced by buoyancy forces) can be observed at each time instance. A comparison of the number of convection cells at the surface with the horizontally averaged instantaneous transfer velocity at $Sc = 200$ is shown in figure 15. As the vast majority of the cells are small, this figure effectively illustrates that the number of small cells is strongly correlated ($\rho((k_L / U_\kappa)_{x,y}, N_c) \geq 0.79$) with the surface-averaged transfer velocity. Correlations of comparable quality, as shown in the figure for $Sc = 200$, were also obtained for $Sc \geq 50$. This indicates that, on average, the contribution of the small cells to the transfer velocity (relative to their surface area) is significantly larger than that of the large cells. This is in accordance with what was observed comparing small to larger, uniformly distributed convection cells for the developing RBM instability (Wissink & Herlina 2023).

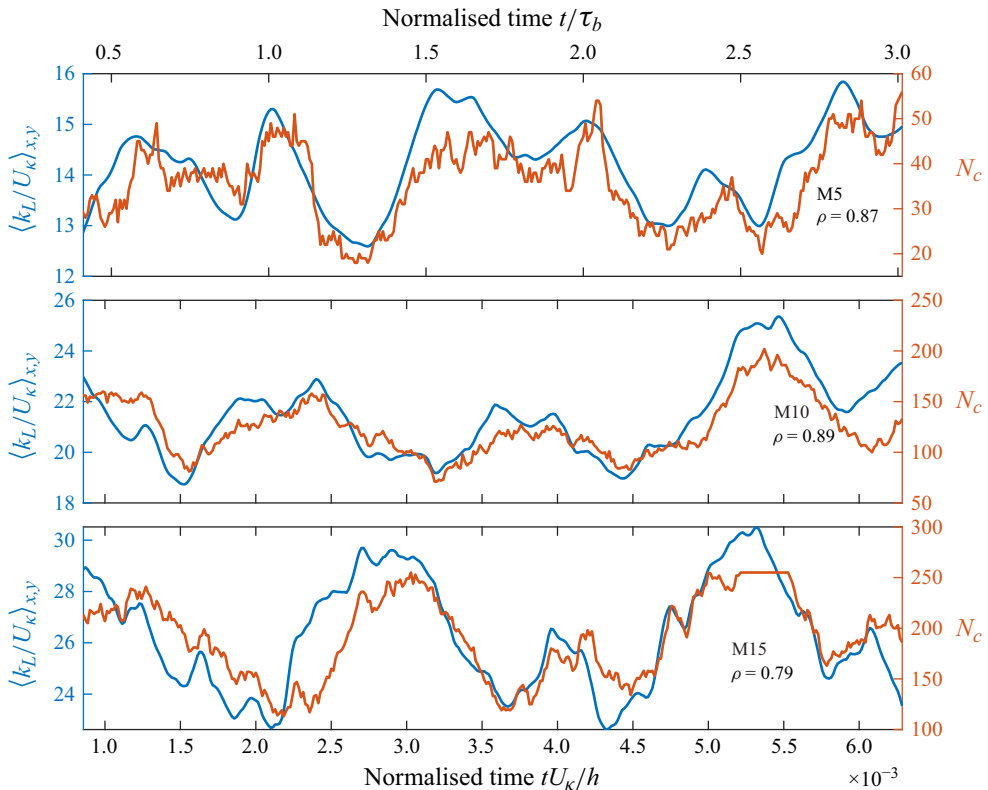


Figure 15. Variation in time of the number of convection cells N_c and the scaled transfer velocity $\langle k_L/U_k \rangle_{x,y}$ at $Sc = 200$ for cases M5, M10 and M15. Also shown are the corresponding correlation coefficients $\rho(\langle k_L \rangle_{x,y}, N_c)$.

After discussing temporal correlations, we now focus on the spatial correlations of surface divergence, temperature and concentrations. Figure 16 shows instantaneous contours of β^* at the surface and T^* , c_{200}^* adjacent to the surface for simulations M0 (upper panes) and M15 (lower panes). While at $Ma_h = 0$ (case M0) the correlation between β^* and T^* is quite good, the quality of this correlation gradually reduces with increasing Ma_h (see figure 17a), resulting in a rather poor correlation at $Ma_h = 13.2 \times 10^5$ (case M15). This deterioration can be explained by the fact that surface tension forces directly depend on surface-temperature gradients. These forces become negligibly small in areas with virtually uniform high or low temperature. Horizontal surface-temperature gradients appear every time warm water moves towards the surface. Subsequently, whilst the generated Marangoni forces move this warm water towards the convection cell edges, it is cooled due to evaporation. At the edges, opposing Marangoni-induced currents from neighbouring convection cells collide and push this now relatively cold surface water downwards ($\beta^* < 0$). As a result, the locations of negative surface divergence remain well correlated with areas of relatively cold water. However, the correlation between areas of warm water and positive surface divergence becomes quite weak. This is because the local Marangoni forces generate strong longitudinal vortices along the edges of convection cells. These vortices not only push cold surface water down but also transport water from the upper bulk upwards. Due to intense mixing and relatively large heat diffusion, this water is

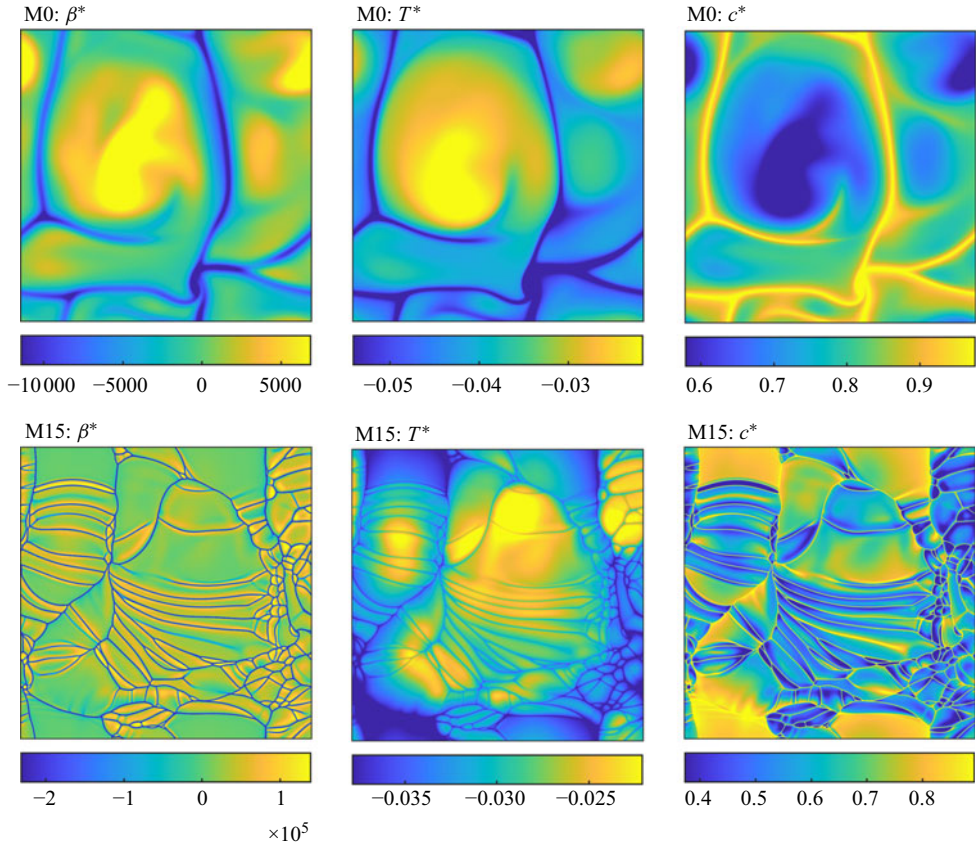


Figure 16. Snapshots showing contours of the surface divergence ($\beta^* = \beta h/U_\kappa$) at the surface and T^* , c_{200}^* , at distances of $\zeta/h = 0.001100$ and $\zeta/h = 0.0005487$ to the surface of simulations M0 with $Ma_h = 0$ (upper panes) and M15 with $Ma_h = 13.21 \times 10^5$ (lower panes), respectively. The contours are extracted at an arbitrary time $t^* = 0.002286$ ($t/\tau_b = 1.1$).

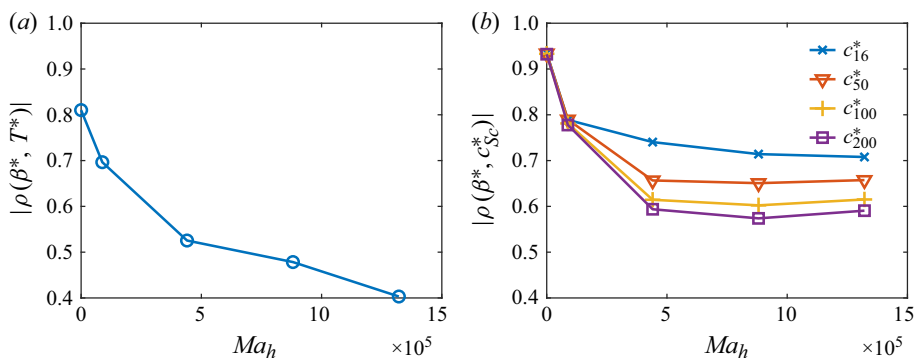


Figure 17. Correlation coefficients between (a) instantaneous surface divergence and temperature fields $\rho(\beta^*, T^*)$, and (b) instantaneous β^* and scalars $\rho(\beta^*, c_{Sc}^*)$ as functions of Marangoni number Ma_h .

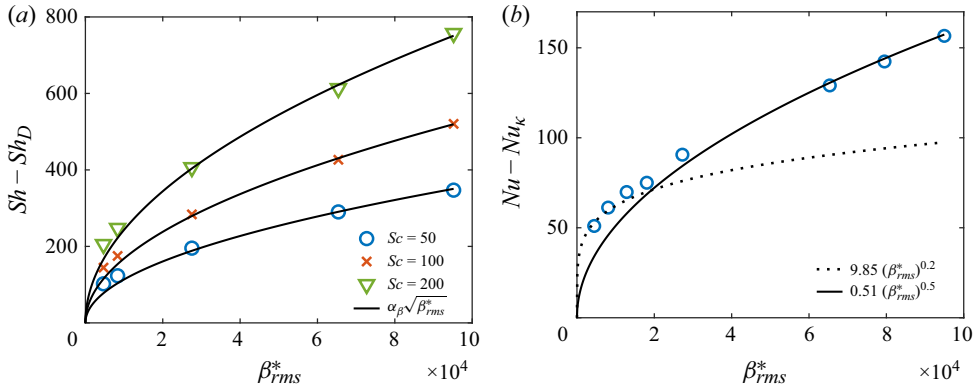


Figure 18. Normalised heat and mass transfer velocities as functions of the surface divergence $\beta_{rms}^* = \beta_{rms} h^2 / \kappa$: (a) $Sh - Sh_D$ vs β_{rms}^* with $a_\beta = 1.14, 1.68, 2.43$, for $Sc = 50, 100, 200$, respectively, and (b) $Nu - Nu_\kappa$ vs β_{rms}^* .

relatively cold compared to the surface water in the middle of the convection cells, thereby adversely affecting $|\rho(\beta^*, T^*)|$.

In contrast to the weak correlation between β^* and T^* for $Ma_h > 0$ mentioned above, the correlation between areas of negative surface divergence (which acts to transport saturated surface water downwards) and areas of relatively high scalar concentration (c_{Sc}^*) is relatively good (cf. figure 16). For the buoyancy-dominated simulations at $Ma_h = 0$ and 0.88×10^5 , the correlations were found to be independent of Sc . In contrast, the Marangoni-dominated simulations ($Ma_h \geq 4.40 \times 10^5$) show a clear reduction in the correlation coefficient with Sc . Initially, starting at $Ma_h = 0$ the correlation was found to worsen with increasing Ma_h before becoming virtually constant for $Ma_h \geq 4.40 \times 10^5$.

Above, the instantaneous spatial correlation coefficients between $-\beta^*$ and c_{200}^* as well as β^* and T^* were shown to be ≥ 0.40 for all $Ma_h \geq 0$. As the near-surface concentration and temperature are directly related to their respective transfer velocities, it is to be expected that the Sherwood number $Sh = K_L h / D$ and the Nusselt number Nu can both be linked to $\beta_{rms}^* = \beta_{rms} h / U_\kappa$. Based on McCready, Vassiliadou & Hanratty (1986), it immediately follows that $Sh \propto \sqrt{\beta_{rms}^*}$. This is confirmed in figure 18(a), which shows results obtained from the mass transfer simulations at $Sc = 50, 100, 200$ as well as their interpolations

$$Sh - Sh_D = a_\beta \sqrt{\beta_{rms}^*}, \quad (3.10)$$

with $a_\beta = 1.14, 1.68, 2.43$ for $Sc = 50, 100, 200$, respectively. It can be seen that, for each Sc , the results obtained for the larger β_{rms}^* (corresponding to the higher Ma_h) are in very good agreement with the interpolating curve. Contrastingly, for the smaller β_{rms}^* , the mass transfer results show a slight deviation, which can be seen to become more pronounced in the corresponding Nusselt number plot (cf. figure 18b). In this figure, for high β_{rms}^* (large Ma_h), the results closely match the

$$Nu - Nu_\kappa = 0.51 (\beta_{rms}^*)^{0.5} \quad (3.11)$$

curve, while the small β_{rms}^* (small Ma_h) results obey a different scaling law:

$$Nu - Nu_\kappa = 9.85 (\beta_{rms}^*)^{0.2}. \quad (3.12)$$

These different scalings can be explained by the fact that the surface divergence β_{rms}^* (which represents the surface velocity frequencies) scales with $U_\sigma/\delta_\sigma \propto Ma_h$ for Marangoni-dominated flows and with $U_R/\delta_R \propto Ra_h^{1.25}$ for fully developed buoyancy-dominated flows (cf. (2.13)–(2.16)). Hence, combined with the results presented in figure 8(a) and (3.3), it immediately follows that for a fully developed flow, the power in the scaling $(Nu - Nu_\kappa) \propto (\beta_{rms}^*)^p$ yields $p = 0.2$ in the buoyancy-dominated regime and $p = 0.5$ in the Marangoni-dominated regime.

4. Conclusions

A series of DNS was performed to study the fully developed RBM instability in a relatively deep domain at a fixed Rayleigh number $Ra_h = 4.44 \times 10^7$ combined with a number of Marangoni numbers ranging from $Ma_h = 0$ to $Ma_h = 13.21 \times 10^5$. The simulations were performed at a fixed Prandtl number of $Pr = 7$, corresponding to water at 20° C. Transfer of gases into the water phase for $Sc = 16\text{--}200$ was calculated for a selected number of Ma_h cases. The results obtained at the highest Schmidt numbers of $Sc = 100, 200$ are deemed to be characteristic also for the transfer of atmospheric gases, of which the Schmidt numbers are of the same order of magnitude. The RBM instability is driven by evaporative cooling at the surface (modelled by a constant heat flux) combined with a fixed temperature at the bottom of the computational domain. The surface of the computational domain was assumed to be flat, while periodic boundary conditions were employed in the horizontal directions.

Visualisation of three-dimensional snapshots showing isosurfaces of the temperature reveal that at all Marangoni numbers there is a quasi-periodic formation of large buoyant plumes of warm water rising up from the bottom of the computational domain. Contrastingly, the thermal boundary layer at the surface was found to be significantly affected by Marangoni forces, especially for $Ma_h \geq 4.40 \times 10^5$. For instance, the typical area of the convection cell footprints (A_c) at the surface was found to drastically reduce with increasing Ma_h according to the scaling $A_c \propto Ma_h^{-1}$. The presence of small long-lived surface-attached plumes was found to be characteristic for the Marangoni-dominated regime. The penetration depth δ_M of these plumes was found to scale with $Ma_h^{-0.5}$. With increasing Ma_h the surface temperature was found to increase, while the temperature in the bulk was found to decrease, resulting in a reduced temperature difference between surface and bulk, and (owing to the same constant heat flux employed in all simulations) also an increase in the heat transfer velocity with Ma_h .

Similar to what was observed for the developing RBM instability in Wissink & Herlina (2023), two regimes were identified. For the lower Marangoni numbers ($Ma_h \leq 2.64 \times 10^5$), the near-surface flow, heat and mass transfer was dominated by buoyancy forces, while for the large Marangoni numbers ($Ma_h > 4.40 \times 10^5$), it is dominated by Marangoni forces. The fact that Ma_{δ_T} was found to significantly increase for small Ma_h to subsequently becoming constant ($Ma_{\delta_T} \approx 53$) for large Ma_h provides conclusive evidence of the existence of the two regimes. A further example of this is the scaling of the non-dimensional heat transfer velocity represented by the Nusselt number

$$(Nu - Nu_\kappa) = a_N (Ma_h + \varepsilon Ra_h)^r, \quad (4.1)$$

where $\varepsilon = 0.0016$, while $[r; a_N] = [0.25; 3.11]$ in the buoyancy-dominated regime and $[r; a_N] = [0.5; 0.13]$ in the Marangoni-dominated regime (cf. figure 8a). Furthermore, in the latter regime, the instantaneous number of convection cells was found to correlate quite well with the instantaneous K_L , which is in agreement with earlier observations that smaller convection cell sizes contribute to higher K_L values.

As was observed above for the heat transfer velocity, increases in Marangoni number (for a fixed Schmidt number Sc) were also found to lead to significant increases in the mass transfer velocity. Because of lack of data, only weak evidence was found for the existence of these two regimes (buoyancy vs Marangoni dominated). It was shown previously that surfactant-induced Marangoni forces significantly inhibit interfacial mass transfer. In the present context, this would correspond to $Ma_h < 0$. Using this notation, the power n in the scaling $K_L \propto Sc^{-n}$ would change from $n = 0.67$ for $Ma_h = -\infty$ to $n = 0.50$ for $Ma_h = 0$. While in the present simulations, where $Ma_h \geq 0$ (promoting interfacial mass transfer), n was found to decrease further from 0.50 to 0.438 as Ma_h was increased from 0 to 13.21×10^5 , respectively. For fixed Ra_h and $Sc \geq 50$, the Schmidt number dependency of K_L could be removed by premultiplying K_L by Sc^n leading to a collapse of the data points obtained for various Schmidt numbers, such that in the buoyancy-dominated regime

$$K_L Sc^n / U_k = 6.12(Ma_h + \varepsilon Ra_h)^{0.25}, \quad (4.2)$$

or equivalently (using the Sherwood number),

$$(Sh - Sh_D) Sc^{n-1} = 0.88(Ma_h + \varepsilon Ra_h)^{0.25}, \quad (4.3)$$

and in the Marangoni-dominated regime

$$K_L Sc^n / U_k = 0.23(Ma_h + \varepsilon Ra_h)^{0.5}, \quad (4.4)$$

or equivalently,

$$(Sh - Sh_D) Sc^{n-1} = 0.033(Ma_h + \varepsilon Ra_h)^{0.5}, \quad (4.5)$$

where n is a function of Ma_h (displayed in figure 14a). Also, in the present fully developed flow, the scaling of both $Sh - Sh_D$ and $Nu - Nu_k$ with $\sqrt{\beta_{rms}^*}$ (cf. (3.10) and (3.11), respectively) as suggested by McCready *et al.* (1986) was found to hold in the Marangoni-dominated regime. To facilitate comparisons with experiments and other numerical simulations, it may be convenient to replace ' $Ma_h + \varepsilon Ra_h$ ' (e.g. in (4.5)) with ' $Bo_h^{-1} + \varepsilon$ ' to obtain an equivalent scaling law.

Acknowledgements. The simulations were performed on the supercomputer bwUniCluster 2.0 and HoreKa supported by the state of Baden-Württemberg through bwHPC.

Funding. This research was partially funded by the German Research Foundation (DFG HE5609/2-1).

Declaration of interests. The authors report no conflict of interest.

Data availability. Data will be made available on request.

Appendix A. Grid resolution requirements

The velocity field was deemed to be fully resolved on the $400 \times 400 \times 252$ base mesh, as for all grid cells, the ratio between the geometrical mean

$$\overline{\Delta} = \sqrt[3]{\Delta x \times \Delta y \times \Delta z} \quad (A1)$$

and the Kolmogorov length scale

$$\eta = (\nu^3 / \epsilon)^{0.25} \quad (A2)$$

was found to be significantly smaller than 1, where

$$\epsilon = \nu \frac{\partial u'_i}{\partial x_j} \frac{\partial u'_i}{\partial x_j} \quad (A3)$$

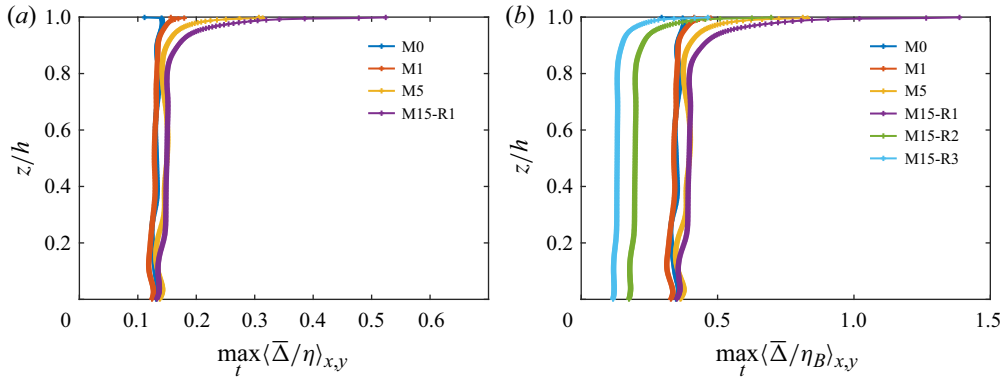


Figure 19. Maximum ratio (obtained during the simulation time) of $\bar{\Delta}$ over (a) the Kolmogorov scale $\langle \eta \rangle_{x,y}$ and (b) the Batchelor scale $\langle \eta_B \rangle_{x,y}$ as obtained for the temperature.

Run	Scalar mesh	$\bar{\Delta}_R$
M15-R1	$400 \times 400 \times 252$	1.41
M15-R2	$800 \times 800 \times 504$	0.73
M15-R3	$1200 \times 1200 \times 756$	0.48

Table 2. Temperature mesh refinement study. The size of the base mesh used in the refinement study for the velocity was $400 \times 400 \times 252$. Here, $\bar{\Delta}_R = \max_{z,t} (\langle \bar{\Delta} / \eta_B \rangle_{x,y})$.

is the dissipation rate of turbulent kinetic energy (cf. figure 19a).

Furthermore, the $400 \times 400 \times 252$ mesh was also found to be sufficiently fine to fully resolve the temperature field in all simulations with $Ma_h < 8.81 \times 10^5$ (cf. table 1). For the more challenging simulations with $Ma_h \geq 8.81 \times 10^5$, a refinement factor of 2 needed to be employed for the temperature field in order for $\bar{\Delta}$ to be smaller than the Batchelor scale

$$\eta_B = \eta Pr^{-0.5} \quad (\text{A4})$$

(cf. figure 19b).

Below, the grid resolution requirements for the active scalar (temperature) in simulation M15 are studied in detail. The meshes used for the temperature are shown in table 2. Each simulation started using the same, fully developed, flow and temperature field and was run for 4 s, corresponding to eight surface-eddy-turnaround times.

As can be seen in figure 20, the instantaneous temperature profiles at $z/h = 0.986$ and $x/h = 2.5$ were found to be in good agreement for R2 and R3, and in reasonable agreement for R1 and R3. Hence, the mesh used in R2 was deemed to be sufficiently fine to accurately resolve the temperature field.

As already mentioned, a base mesh refinement factor of $R = 2$ was also the smallest refinement factor needed to ensure that the ratio

$$\bar{\Delta}_R = \max_{z,t} \left\langle \frac{\bar{\Delta}}{\eta_B} \right\rangle_{x,y} < 1. \quad (\text{A5})$$

Note that as the temperature is an active scalar and directly influences the velocity field, it is important to use the same mesh to resolve both the velocity and the temperature.

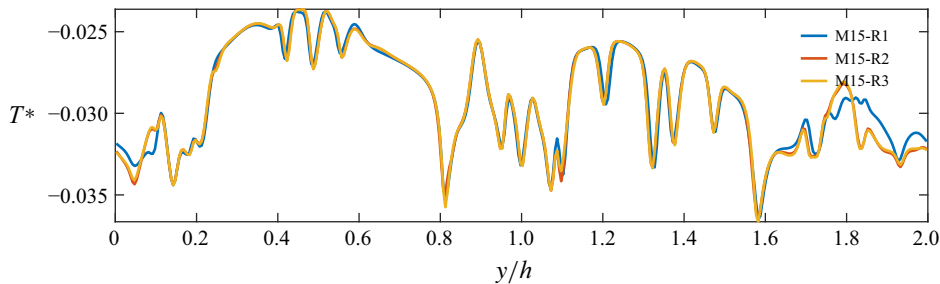


Figure 20. Temperature profiles obtained after about eight surface-eddy-turnaround times at $x/h = 2.5$ and $z/h = 0.986$ using different refinements of the base mesh.

Hence, it was decided to use a $800 \times 800 \times 504$ base mesh for all simulations with $Ma_h \geq 8.81 \times 10^5$, without any further refinement for the temperature ($R = 1$).

Subsequently, the resolution requirements for a scalar with Schmidt number Sc was determined by choosing a refinement factor R such that $\bar{\Delta}_R$ is less than one, where η_B was estimated using

$$\eta_B = \eta Sc^{-0.5}. \quad (\text{A6})$$

The various refinement factors employed for the scalars can be seen in table 1).

REFERENCES

ALI, F. 2020 Methods for surface age estimation and study of evaporative cooling induced air-water gas transfer PhD thesis. Brunel University London.

BALACHANDAR, S. 1992 Structure of turbulent thermal convection. *Phys. Fluids A* **4**, 2715.

BLOMQUIST, B.W., *et al.* 2017 Wind speed and sea state dependencies of air-sea gas transfer: results from the high wind speed gas exchange study (HiWinGS). *J. Geophys. Res.: Oceans* **122** (10), 8034–8062.

BODENSCHATZ, E., PESCH, W. & AHLERS, G. 2000 Recent developments in Rayleigh–Bénard convection. *Annu Rev. Fluid Mech.* **32** (1), 709–778.

CHENG, L., *et al.* 2022 Past and future ocean warming. *Nat. Rev. Earth Environ.* **3** (11), 776–794.

DAVENPORT, I.F. 1972 The initiation of natural convection caused by time-dependent profiles, Dissertation. Lawrence Berkeley National Laboratory.

DHAS, D.J., ROY, A. & TOPPALADODDI, S. 2023 Penetrative and marangoni convection in a fluid film over a phase boundary. *J. Fluid Mech.* **977**, A34.

DIDDEN, C., LI, Y. & LOHSE, D. 2021 Competing Marangoni and Rayleigh convection in evaporating binary droplets. *J. Fluid Mech.* **914**, A23.

DUDA, J.L. & VRENTAS, J.S. 1968 Laminar liquid jet diffusion studies. *AIChE J.* **14** (2), 286–294.

FISCHER, H.B., LIST, E.J., KOH, R.C.Y. & IMBERGER, J.B.N.H. 1979 *Mixing in Inland and Coastal Waters*. Academic Press.

FLACK, K.A., SAYLOR, J.R. & SMITH, G.B. 2001 Near-surface turbulence for evaporative convection at an air/water interface. *Phys. Fluids* **13** (11), 3338–3345.

GARBE, C.S., RUTGERSSON, A., BOUTIN, J., DE LEEUW, G., *et al.* 2014 Transfer across the air-sea interface. In *Ocean-Atmosphere Interactions of Gases and Particles*, LISS, P.S. & JOHNSON, M.T. (eds), Springer Earth System Sciences.

GRUBER, N., BAKKER, D.C., DEVRIES, T., GREGOR, L., HAUCK, J., LANDSCHÜTZER, P., MCKINLEY, G.A. & MÜLLER, J.D. 2023 Trends and variability in the ocean carbon sink. *Nat. Rev. Earth Environ.* **4** (2), 119–134.

HERLINA, & JIRKA, G.H. 2008 Experiments on gas transfer at the air-water interface induced by oscillating grid turbulence. *J. Fluid Mech.* **594**, 183–208.

HERLINA, H. & WISSINK, J.G. 2014 Direct numerical simulation of turbulent scalar transport across a flat surface. *J. Fluid Mech.* **744**, 217–249.

HERLINA, H. & WISSINK, J.G. 2019 Simulation of air-water interfacial mass transfer driven by high-intensity isotropic turbulence. *J. Fluid Mech.* **860**, 419–440.

HUOTARI, J., HAAPANALA, S., PUMPANEN, J., VESALA, T. & OJALA, A. 2013 Efficient gas exchange between a boreal river and the atmosphere. *Geophys. Res. Lett.* **40** (21), 5683–5686.

JÄHNE, B. & HAUSSECKER, H. 1998 Air-water gas exchange. *Annu. Rev. Fluid Mech.* **30**, 443–468.

JIRKA, G.H., HERLINA, H. & NIEPELT, A. 2010 Gas transfer at the air-water interface: experiments with different turbulence forcing mechanisms. *Exp. Fluids* **49** (1), 319–327.

JOHNSON, G.C., *et al.* 2021 Global oceans. *B. Am. Meteorol. Soc.* **102** (8), S143–S198.

KHAKPOUR, H.R., SHEN, L. & YUE, D.K.P. 2011 Transport of passive scalar in turbulent shear flow under a clean or surfactant-contaminated free surface. *J. Fluid Mech.* **670**, 527–557.

KÖLLNER, T., SCHWARZENBERGER, K., ECKERT, K. & BOECK, T. 2016 The eruptive regime of mass-transfer-driven Rayleigh–Marangoni convection. *J. Fluid Mech.* **791**, R4.

KOMORI, S., IWANO, K., TAKAGAKI, N., ONISHI, R., KUROSE, R., TAKAHASHI, K. & SUZUKI, N. 2018 Laboratory measurements of heat transfer and drag coefficients at extremely high wind speeds. *J. Phys. Ocean.* **48** (4), 959–974.

KOSCHMIEDER, E.L. & PRAHL, S.A. 1990 Surface-tension-driven Bénard convection in small containers. *J. Fluid Mech.* **215**, 571–583.

KUBRAK, B., HERLINA, H., GREVE, F. & WISSINK, J.G. 2013 Low-diffusivity scalar transport using a WENO scheme and dual meshing. *J. Comput. Phys.* **240**, 158–173.

KUROSE, R., TAKAGAKI, N., KIMURA, A. & KOMORI, S. 2016 Direct numerical simulation of turbulent heat transfer across a sheared wind-driven gas–liquid interface. *J. Fluid Mech.* **804**, 646–687.

LEDWELL, J.J. 1984 The variation of the gas transfer coefficient with molecular diffusity. In *Gas Transfer at Water Surfaces*, pp. 293–302. Springer.

LIU, X., OSHER, S. & CHAN, T. 1994 Weighted essentially non-oscillatory schemes. *J. Comput. Phys.* **115** (1), 200–212.

MACINTYRE, S., AMARAL, J.H.F. & MELACK, J.M. 2021 Enhanced turbulence in the upper mixed layer under light winds and heating: implications for gas fluxes. *J. Geophys. Res.: Oceans* **126** (12), e2020JC017026.

MACINTYRE, S., CROWE, A.T., CORTÉS, A. & ARNEBORG, L. 2018 Turbulence in a small arctic pond. *Limnol. Oceanogr.* **63** (6), 2337–2358.

MAGNAUDET, J. & CALMET, I. 2006 Turbulent mass transfer through a flat shear-free surface. *J. Fluid Mech.* **553**, 155–185.

MCCREADY, M.J., VASSILIADOU, E. & HANRATTY, T.J. 1986 Computer-simulation of turbulent mass-transfer at a mobile interface. *AIChE J.* **32** (7), 1108–1115.

MCKENNA, S.P. & MCGILLIS, W.R. 2004 The role of free-surface turbulence and surfactants in air-water gas transfer. *Int. J. Heat Mass Tran.* **47** (3), 539–553.

MURNIATI, E., PHILIPPE, A., EIFF, O. & HERLINA, H. 2025 A combined intensity and lifetime-based laser-induced fluorescence technique (i - τ LIF) with dye-doped nanobeads tracer for dissolved oxygen imaging below the water surface. *Exp. Fluids* **66** (7), 1–19.

NAGAOSA, R. & HANDLER, R.A. 2012 Characteristic time scales for predicting the scalar flux at a free surface in turbulent open channel flow. *AIChE* **58**, 3867–3877.

NEPOMNYASHCHY, A., LEGROS, J.C. & SIMANOVSKII, I. 2006 *Interfacial Convection in Multilayer Systems*. Springer.

NIELD, D.A. 1964 Surface tension and buoyancy effects in cellular convection. *J. Fluid Mech.* **19** (3), 341–352.

PAN, Y., *et al.* 2023 Annual cycle in upper-ocean heat content and the global energy budget. *J. Climate* **36** (15), 5003–5026.

PEARSON, J.R.A. 1958 On convection cells induced by surface tension. *J. Fluid Mech.* **4** (5), 489–500.

PINELLI, M., HERLINA, H., WISSINK, J.G. & UHLMANN, M. 2022 Direct numerical simulation of turbulent mass transfer at the surface of an open channel flow. *J. Fluid Mech.* **933**, A49.

PODGRAJSEK, E., SAHLEE, E. & RUTGERSSON, A. 2014 Diurnal cycle of lake methane flux. *J. Geophys. Res. Biogeosci.* **119** (3), 236–248.

RUTGERSSON, A. & SMEDMAN, A. 2010 Enhanced air-sea CO_2 transfer due to water-side convection. *J. Marine Syst.* **80** (1–2), 125–134.

SCHLADOW, S.G., LEE, M., HÜRZELER, B.E. & KELLY, P.B. 2002 Oxygen transfer across the air-water interface by natural convection in lakes. *Limnol. Ocean.* **47** (5), 1394–1404.

SCHWARZENBERGER, K., KÖLLNER, T., LINDE, H., BOECK, T., ODENBACH, S. & ECKERT, K. 2014 Pattern formation and mass transfer under stationary solutal Marangoni instability. *Adv. Colloid Interface Sci.* **206**, 344–371.

SCHWERTFIRM, F. & MANHART, M. 2007 DNS of passive scalar transport in turbulent channel flow at high Schmidt numbers. *Int. J. Heat Fluid Fl.* **28**, 1204–1214.

SHAY, T.J. & GREGG, M.C. 1984 Turbulence in an oceanic convective mixed layer. *Nature* **310** (5975), 282–285.

SHEN, L., YUE, D.K.P. & TRIANTAFYLLOU, G.S. 2004 Effect of surfactants on free-surface turbulent flows. *J. Fluid Mech.* **506**, 79–115.

SOLOVIEV, A. & KLINGER, B. 2001 Open ocean convection.

SPANGENBERG, W.G. & ROWLAND, W.R. 1961 Convective circulation in water induced by evaporative cooling. *Phys. Fluids* **4** (6), 743.

TAN, K.K. & THORPE, R.B. 1996 The onset of convection caused by buoyancy during transient heat conduction in deep fluids. *Chem. Engng. Sci.* **51** (17), 4127–4136.

TOUSSAINT, G., BODIGUEL, H., DOUMENC, F., GUERRIER, B. & ALLAIN, C. 2008 Experimental characterization of buoyancy- and surface tension-driven convection during the drying of a polymer solution. *Int. J. Heat Mass Trans.* **51** (17), 4228–4237.

TSAI, W.-T., CHEN, S.-M., LU, G.-H. & GARBE, C.S. 2013 Characteristics of interfacial signatures on a wind-driven gravity-capillary wave. *J. Geophys. Res.: Oceans* **118** (4), 1715–1735.

TURNEY, D.E. 2016 Coherent motions and time scales that control heat and mass transfer at wind-swept water surfaces. *J. Geophys. Res.: Oceans* **121** (12), 8731–8748.

TURNEY, D.E. & BANERJEE, S. 2013 Air-water gas transfer and near-surface motions. *J. Fluid Mech.* **733**, 588–624.

VARIANO, E.A. & COWEN, E.A. 2013 Turbulent transport of a high-Schmidt-number scalar near an air–water interface. *J. Fluid Mech.* **731**, 259–287.

WANNINKHOF, R. 2014 Relationship between wind speed and gas exchange over the ocean revisited. *Limnol. Ocean: Methods* **12** (6), 351–362.

WISSINK, J.G. 2004 On unconditional conservation of kinetic energy by finite-difference discretisations of the linear and non-linear convection equation. *Comput. Fluids* **33**, 315–343.

WISSINK, J.G. & HERLINA, H. 2016 Direct numerical simulation of gas transfer across the air-water interface driven by buoyant convection. *J. Fluid Mech.* **787**, 508–540.

WISSINK, J.G. & HERLINA, H. 2023 Surface-temperature-induced Marangoni effects on developing buoyancy-driven flow. *J. Fluid Mech.* **962**, A23.

WISSINK, J.G., HERLINA, H., AKAR, Y. & UHLMANN, M. 2017 Effect of surface contamination on interfacial mass transfer rate. *J. Fluid Mech.* **830**, 5–34.

YU, L. 2019 Global air–sea fluxes of heat, fresh water, and momentum: energy budget closure and unanswered questions. *Ann. Rev. Marine Sci.* **11** (1), 227–248.

ZAPPA, C.J., MCGILLIS, W.R., RAYMOND, P.A., EDSON, J.B., HINTSA, E.J., ZEMMELINK, H.J., DACEY, J.W.H. & HO, D.T. 2007 Environmental turbulent mixing controls on air-water gas exchange in marine and aquatic systems. *Geophys. Res. Lett.* **34** (10).